Draft version May 8, 2025
Typeset using LaTeX twocolumn style in AASTeX7

arXiv:2505.04609v1 [astro-ph.GA] 7 May 2025

CAPERS-LRD-z9: A Gas Enshrouded Little Red Dot Hosting a Broad-line AGN at $z = 9.288$

Anthony J. Taylor [1], Vasily Kokorev [1], Dale D. Kocevski [2], Hollis B. Akins [1], Fergus Cullen [3], Mark Dickinson [4], Steven L. Finkelstein [1], Pablo Arrabal Haro [5,*], Volker Bromm [1], Mauro Giavalisco [6], Kohei Inayoshi [7], Stéphanie Juneau [4], Gene C. K. Leung [8], Pablo G. Pérez-González [9], Rachel S. Somerville [10], Jonathan R. Trump [11], Ricardo O. Amorín [12], Guillermo Barro [13], Denis Burgarella [14], Madisyn Brooks [11], Adam Carnall [3], Caitlin M. Casey [15,16], Yingjie Cheng [6], John Chisholm [1], Katherine Chworowsky [1,†], Kelcey Davis [11,‡], Callum T. Donnan [4], James S. Dunlop [3], Richard S. Ellis [17], Vital Fernández [18], Seiji Fujimoto [1], Norman A. Grogin [19], Ansh R. Gupta [1,‡], Nimish P. Hathi [19], Intae Jung [19], Michaela Hirschmann [20], Jeyhan S. Kartaltepe [21], Anton M. Koekemoer [19], Rebecca L. Larson [19], Ho-Hin Leung [3], Mario Llerena [22], Ray A. Lucas [19], Derek J. McLeod [3], Ross McLure [3], Lorenzo Napolitano [22,23], Casey Papovich [24,25], Thomas M. Stanton [3], Roberta Tripodi [22,26], Xin Wang [27,28,29], Stephen M. Wilkins [30,31], L. Y. Aaron Yung [19] and Jorge A. Zavala [6]

[1] *Department of Astronomy, The University of Texas at Austin, Austin, TX, USA*
[2] *Department of Physics and Astronomy, Colby College, Waterville, ME 04901, USA*
[3] *Institute for Astronomy, University of Edinburgh, Royal Observatory, Edinburgh EH9 3HJ, UK*
[4] *NSF's National Optical-Infrared Astronomy Research Laboratory, 950 N. Cherry Ave., Tucson, AZ 85719, USA*
[5] *Astrophysics Science Division, NASA Goddard Space Flight Center, 8800 Greenbelt Rd, Greenbelt, MD 20771, USA*
[6] *University of Massachusetts Amherst, 710 North Pleasant Street, Amherst, MA 01003-9305, USA*
[7] *Kavli Institute for Astronomy and Astrophysics, Peking University, Beijing 100871, China*
[8] *MIT Kavli Institute for Astrophysics and Space Research, 77 Massachusetts Ave., Cambridge, MA 02139, USA*
[9] *Centro de Astrobiología (CAB), CSIC-INTA, Ctra. de Ajalvir km 4, Torrejón de Ardoz, E-28850, Madrid, Spain*
[10] *Center for Computational Astrophysics, Flatiron Institute, 162 5th Avenue, New York, NY, 10010, USA*
[11] *Department of Physics, 196 Auditorium Road, Unit 3046, University of Connecticut, Storrs, CT 06269, USA*
[12] *Instituto de Astrofísica de Andalucía (CSIC), Apartado 3004, 18080 Granada, Spain*
[13] *Department of Physics, University of the Pacific, Stockton, CA 90340 USA*
[14] *Aix Marseille Univ, CNRS, CNES, LAM Marseille, France*
[15] *Department of Physics, University of California, Santa Barbara, CA 93106, USA*
[16] *Cosmic Dawn Center (DAWN), Niels Bohr Institute, University of Copenhagen, Jagtvej 128, København N, DK-2200, Denmark*
[17] *Department of Physics and Astronomy, University College London, Gower Street, London WC1E 6BT, UK*
[18] *Michigan Institute for Data Science, Unversity of Michigan, 500 Church Street, Ann Arbor, MI 48109, USA*
[19] *Space Telescope Science Institute, 3700 San Martin Drive, Baltimore, MD 21218, USA*
[20] *Institute of Physics, Laboratory of Galaxy Evolution, Ecole Polytechnique Federale de Lausanne (EPFL), Observatoire de Sauverny, 1290 Versoix, Switzerland*
[21] *Laboratory for Multiwavelength Astrophysics, School of Physics and Astronomy, Rochester Institute of Technology, 84 Lomb Memorial Drive, Rochester, NY 14623, USA*
[22] *INAF - Osservatorio Astronomico di Roma, via Frascati 33, 00078, Monte Porzio Catone, Italy*
[23] *Dipartimento di Fisica, Università di Roma Sapienza, Città Universitaria di Roma - Sapienza, Piazzale Aldo Moro, 2, 00185, Roma, Italy*
[24] *Department of Physics and Astronomy, Texas A&M University, College Station, TX, 77843-4242 USA*
[25] *George P. and Cynthia Woods Mitchell Institute for Fundamental Physics and Astronomy, Texas A&M University, College Station, TX, 77843-4242 USA*
[26] *IFPU - Institute for Fundamental Physics of the Universe, Via Beirut 2, I-34014 Trieste, Italy*
[27] *School of Astronomy and Space Science, University of Chinese Academy of Sciences (UCAS), Beijing 100049, China*
[28] *National Astronomical Observatories, Chinese Academy of Sciences, Beijing 100101, China*
[29] *Institute for Frontiers in Astronomy and Astrophysics, Beijing Normal University, Beijing 102206, China*
[30] *Astronomy Centre, University of Sussex, Falmer, Brighton BN1 9QH, UK*
[31] *Institute of Space Sciences and Astronomy, University of Malta, Msida MSD 2080, Malta*

Corresponding author: Anthony J. Taylor
anthony.taylor@austin.utexas.edu

ABSTRACT

We present CAPERS-LRD-z9, a little red dot (LRD) which we confirm to be a $z = 9.288$ broad-line AGN (BLAGN). First identified as a high-redshift LRD candidate from PRIMER NIRCam photometry, follow-up NIRSpec/PRISM spectroscopy of CAPERS-LRD-z9 from the CANDELS-Area Prism Epoch of Reionization Survey (CAPERS) has revealed a broad 3500 km s^{-1} Hβ emission line and narrow [O III]$\lambda\lambda$4959, 5007 lines, indicative of a BLAGN. Based on the broad Hβ line, we compute a canonical black-hole mass of $\log(M_{\rm BH}/M_\odot) = 7.58 \pm 0.15$, although full consideration of systematic uncertainties yields a conservative range of $6.65 < \log(M_{\rm BH}/M_\odot) < 8.50$. These observations suggest that either a massive black hole seed, or a lighter stellar remnant seed undergoing periods of super-Eddington accretion, is necessary to grow such a massive black hole in $\lesssim 500$ Myr of cosmic time. CAPERS-LRD-z9 exhibits a strong Balmer break, consistent with a central AGN surrounded by dense ($\sim 10^{10}$ cm^{-3}) neutral gas. We model CAPERS-LRD-z9 using `CLOUDY` to fit the emission red-ward of the Balmer break with a dense gas-enshrouded AGN, and `bagpipes` to fit the rest-ultraviolet emission as a host-galaxy stellar population. This upper limit on the stellar mass of the host galaxy ($< 10^9$ M$_\odot$) implies that the black-hole to stellar mass ratio may be extremely large, possibly $> 5\%$ (although systematic uncertainties on the black-hole mass prevent strong conclusions). However, the shape of the UV continuum differs from typical high-redshift star-forming galaxies, indicating that this UV emission may also be of AGN origin, and hence the true stellar mass of the host may be still lower.

1. INTRODUCTION

In the years following its launch, *JWST* has uncovered previously inaccessible populations of galaxies. These objects include an unprecedented population of galaxies at redshifts of $z > 10$ (e.g., S. L. Finkelstein et al. 2022; M. Castellano et al. 2022; R. P. Naidu et al. 2022; P. Arrabal Haro et al. 2023; B. E. Robertson et al. 2023; B. Wang et al. 2023; S. Carniani et al. 2024; C. T. Donnan et al. 2024; V. Kokorev et al. 2025; J. A. Zavala et al. 2025), and a surprisingly large population of broad-line active galactic nuclei (BLAGN) at $z \gtrsim 6$ (e.g., R. L. Larson et al. 2023; A. J. Bunker et al. 2023; D. D. Kocevski et al. 2023; Y. Harikane et al. 2023; D. D. Kocevski et al. 2025; R. Maiolino et al. 2023; H. B. Akins et al. 2024; J. Matthee et al. 2024; L. J. Furtak et al. 2024; I. Juodžbalis et al. 2024; V. Kokorev et al. 2023; R. Tripodi et al. 2024; A. J. Taylor et al. 2024; B. Wang et al. 2024a; I. Juodžbalis et al. 2024, 2025; H. B. Akins et al. 2025a).

One of the more enigmatic populations identified by *JWST* are the red compact objects that have been named "Little Red Dots" (LRDs; J. Matthee et al. 2024). These sources were first identified photometrically due to their compact morphology and unique "v-shaped" spectral energy distributions (SEDs), which feature a steep red continuum in the rest-frame optical, with relatively blue colors in the rest-frame UV (D. D. Kocevski et al. 2023; G. Barro et al. 2023; I. Labbé et al. 2023). Subsequent spectroscopic observations have revealed that $\gtrsim 60\%$ of these sources exhibit broad Balmer emission lines, which when coupled with narrow observed forbidden lines is indicative of BLAGN (D. D. Kocevski et al. 2023; V. Kokorev et al. 2023; L. J. Furtak et al. 2024; J. E. Greene et al. 2024; J. Matthee et al. 2024; D. D. Kocevski et al. 2025). While alternative explanations for these broad-line features have been proposed (e.g., J. F. W. Baggen et al. 2024), several lines of evidence such as high-ionization lines (I. Labbe et al. 2024; R. Tripodi et al. 2024; H. B. Akins et al. 2025a) and Balmer absorption (J. Matthee et al. 2024; X. Ji et al. 2025) point to an AGN powering a significant fraction of the rest-frame optical emission.

LRDs have been shown to be numerous, making up $\sim 20-30\%$ of the BLAGN identified by JWST at $z > 3$ (Y. Harikane et al. 2023; J. E. Greene et al. 2024; R. Maiolino et al. 2024; A. J. Taylor et al. 2024). Their number density matches or exceeds the total pre-*JWST* expected contribution of UV-faint ($M_{UV} > -21$) AGN to the UV luminosity function at $4.5 < z < 8.5$, and LRDs represent $\sim 1\%$ of the total galaxy UVLF over the same range (S. L. Finkelstein & M. B. Bagley 2022; V. Kokorev et al. 2024a; D. D. Kocevski et al. 2025; A. J. Taylor et al. 2024). Under the broad-line AGN interpretation, LRDs host supermassive black holes (SMBHs) with some reaching $M_{\rm BH} > 10^7 M_\odot$ within the first Gyr of cosmic time. These objects thus provide insight into black hole seeding and growth in the early universe (e.g., A. Smith & V. Bromm 2019; T. E. Woods et al. 2019; K. Inayoshi et al. 2020; J. Regan & M. Volonteri 2024; J. Jeon et al. 2025a).

* NASA Postdoctoral Fellow
† NSF Graduate Fellow
‡ NSF Graduate Research Fellow

However, analysis of the rest-frame near-infrared (near-IR), or observed mid-infrared (mid-IR), emission of LRDs further complicates their physical interpretation. Observations with JWST/MIRI have shown a surprisingly flat continuum at rest-frame $1-3\mu$m (e.g., C. C. Williams et al. 2024; P. G. Pérez-González et al. 2024; H. B. Akins et al. 2024; G. C. K. Leung et al. 2024; G. Barro et al. 2024), suggesting a lack of a hot dusty torus commonly seen in reddened AGNs at up to $z \sim 6$ (e.g., R. Barvainis 1987; J. Lyu & G. Rieke 2022). Full SED analysis using NIRCam and MIRI shows either no correlation (G. C. K. Leung et al. 2024) or a negative correlation (G. Barro et al. 2024) between the apparent extinction in LRDs and their rest-MIR emission, indicating an alternative source of obscuration than hot dust. Moreover, applying a conventional AGN SED model with dust obscuration implies highly over-massive black holes in LRDs, hinting at either some stellar contribution or super-Eddington accretion (G. C. K. Leung et al. 2024).

A subset of LRDs with deep *JWST*/NIRSpec PRISM spectroscopy exhibit strong Balmer breaks (e.g., B. Wang et al. 2024b; D. J. Setton et al. 2024). While this initially suggested that the emission at these wavelengths must be dominated by stars, some of these objects exhibit greater break strengths than are possible from an evolved stellar population alone (e.g., C. C. Williams et al. 2024; I. Labbe et al. 2024; X. Ji et al. 2025; A. de Graaff et al. 2025; R. P. Naidu et al. 2025), thus requiring an alternative explanation. K. Inayoshi & R. Maiolino (2025) suggest that generating such breaks is in fact possible without stellar emission, by instead modeling an AGN enshrouded by a cocoon of dense neutral gas. In this model, the high column density of this gas results in a significant population of $n = 2$ collisionally excited state hydrogen atoms that resonantly scatter Balmer line emission, and absorb and reprocess light at wavelengths less than the Balmer limit ($\sim$3650 Å), much like photons blueward of the Lyman limit in less-dense gas where the bulk of hydrogen atoms are in the ground state. This results in a stronger Balmer break, and narrow absorption features superimposed upon the broad Balmer emission lines. These absorption features have indeed been identified in several LRDs (J. Matthee et al. 2024; D. D. Kocevski et al. 2025; A. J. Taylor et al. 2024; B. Wang et al. 2024a; X. Ji et al. 2025; A. de Graaff et al. 2025; V. Rusakov et al. 2025; R. P. Naidu et al. 2025). This theory also helps explain the lack of X-ray emission exhibited by LRDs due to Compton-thick absorption (D. D. Kocevski et al. 2025; M. Yue et al. 2024a; R. Maiolino et al. 2025) as well as the higher Balmer decrements observed from broad lines compared to narrow lines (e.g., M. Brooks et al. 2024; R. P. Naidu et al. 2025).

The origin and growth histories of these supermassive black holes remains an open puzzle (K. Inayoshi et al. 2020; M. Volonteri et al. 2021). The most commonly considered scenarios for creating seed black holes can be divided into two categories: 1) Light seeds ($m_{\rm seed} \sim 100\,M_\odot$), left behind as stellar remnants of massive Population III (Pop III) stars, and 2) Heavy seeds, which may form via runaway collisions in dense environments such as stellar clusters (thought to create seeds with $m_{\rm seed} \sim 10^3$–$10^4\,M_\odot$, which may rapidly grow to $\sim 10^5$–$10^6\,M_\odot$ via mergers), or via direct collapse of primordial gas clouds under special conditions such as strong Lyman-Werner (LW) radiation fields, high baryon-DM streaming velocity, or gas-rich mergers, leading to seeds with masses $m_{\rm seed} \sim 10^5$–$10^6\,M_\odot$ (see review by K. Inayoshi et al. 2020, and references therein). A more exotic origin for seed BHs, involving a qualitatively different evolutionary sequence, is primordial black holes that form shortly after the Big Bang (e.g., B. Liu & V. Bromm 2022; S. Zhang et al. 2025; F. Ziparo et al. 2025; A. Matteri et al. 2025). It is possible, even likely, that multiple mechanisms contribute to seeding the black hole population that we observe.

In order to reach the masses of the detected high redshift black holes, light seeds must grow at or above the Eddington rate with a high duty cycle from an early epoch ($z \gtrsim 20$). Heavier seeds can grow at more moderate rates. For the broader category of non-LRD broad line high redshift AGN, the estimated BH masses appear to make many of these objects "over-massive" compared to their stellar hosts, with black hole to stellar mass ratios far above the typical $M_{\rm BH}/M_* \sim 0.1\%$ exhibited by local dormant black holes and AGN (B. Agarwal et al. 2013; F. Pacucci et al. 2023). However, we note that analyzing this "over-massiveness" on a population level may be subject to Lauer bias (T. R. Lauer et al. 2007; J. Li et al. 2025). The stellar masses of LRDs are particularly uncertain, given that it is unknown whether the observed UV light comes from the AGN or the stars, but some estimates suggest that they may have some of the most extreme over-massive BHs, with some approaching $\sim 10-100\%$ of the host galaxy's stellar mass (e.g. R. Maiolino et al. 2023; V. Kokorev et al. 2023; D. D. Kocevski et al. 2025; C.-H. Chen et al. 2025). Heavy seeds would provide one obvious explanation for over-massive black holes, but there are other explanations such as periods of more rapid growth of the BH relative to the stars, or selection effects. Pushing black hole detections to earlier cosmic epochs, closer to the presumed epoch of BH seeding, is one of the most promising avenues to dis-

entangle the degeneracies between seeding and accretion physics.

These numerous open questions have prompted ongoing campaigns for spectroscopic followup of photometrically identified LRDs, especially those at high photometric redshifts ($z \gtrsim 9$). Here, we present CAPERS-LRD-z9, the highest redshift spectroscopically confirmed LRD and BLAGN yet discovered. The source was first identified as a high-z LRD candidate in D. D. Kocevski et al. (2025) and subsequently also selected by G. Barro et al. (2024) and H. B. Akins et al. (2024). It was also independently selected as a galaxy candidate at $z = 9 - 10$ by C. T. Donnan et al. (2024). We now observe this source using NIRSpec observations taken as part of the CANDELS-Area Prism Epoch of Reionization Survey (CAPERS) program (GO-6368; PI. M. Dickinson).

This paper is organized as follows. First, in §2, we describe the *JWST* NIRCam, NIRSpec, and MIRI data used in the discovery and follow-up of CAPERS-LRD-z9. In §3, we describe our measurements of the spectroscopic redshift, emission-line properties, morphology, Balmer decrement, and Balmer break in CAPERS-LRD-z9. In §4, we compute the black hole and stellar masses of CAPERS-LRD-z9, and we discuss the implications of these properties and the applicability of the dense neutral gas model of LRDs to this source. Finally, we summarize our work in §6. We assume a flat Λ cold dark matter cosmology with Ω_m=0.3, Ω_Λ=0.7, and H_0=70 km s^{-1} Mpc^{-1} throughout. All magnitudes are given in the AB magnitude system, where an AB magnitude is defined by $m_{\rm AB}=-2.5\log f_\nu - 48.60$. Here, f_ν is the specific flux density of the source in units of erg cm^{-2} s^{-1} Hz^{-1}.

2. OBSERVATIONS AND DATA REDUCTION

CAPERS-LRD-z9 was first identified as a potential very high redshift LRD from the *JWST* NIRCam imaging provided by the PRIMER survey (J. S. Dunlop et al. 2021) in the COSMOS field (D. D. Kocevski et al. 2025; G. Barro et al. 2024; H. B. Akins et al. 2024). The LRD selection was based on an analysis of the rest-frame UV and optical spectral energy distribution (SED) slopes following determination of the source's photometric redshift with `EAZY` (G. B. Brammer et al. 2008). As potentially the highest redshift LRD discovered to date, CAPERS-LRD-z9 was identified as a high-value target for CAPERS, and therefore it was selected to receive a slitlet and a full-depth CAPERS integration (see §2.1). While the full details of CAPERS target selection, data reduction, and program design will be described in future works, we summarize the observations below.

2.1. *NIRSpec Observations*

CAPERS is a *JWST* Cycle-3 Legacy program which uses NIRSpec/MSA/PRISM to observe very high-redshift galaxies, AGN candidates, and other objects of community interest in three of the CANDELS legacy fields (N. A. Grogin et al. 2011; A. M. Koekemoer et al. 2011) as identified from the deep multi-band NIRCam imaging provided by the Public Release IMaging for Extragalactic Research (PRIMER; Dunlop et al. in preparation) and the Cosmic Evolution Early Release Science (CEERS; S. L. Finkelstein et al. 2025) *JWST* surveys.

CAPERS is targeting seven MSA pointings in each of the PRIMER-UDS, PRIMER-COSMOS, and Extended Groth Strip (EGS) fields, observing three MSA configurations at each pointing. This multi-configuration approach allows CAPERS to observe high-value targets in multiple configurations to increase their exposure times, while simultaneously observing a large number of other targets in each individual configuration to increase the overall sample yield. As a high-value target, CAPERS-LRD-z9 (a.k.a. CAPERS-COSMOS-119334) was observed in all three configurations executed in CAPERS COSMOS pointing P4. These observations targeting CAPERS-LRD-z9 were executed on 2025 April 15 using two iterations of a standard three-shutter nodding scheme per MSA configuration for a total of 18 exposures at a NIRSpec aperture position angle (east of north) of 246.585°. Each of these 18 nods was observed for a single 13 group integration using the `NRSIRS2` readout pattern for a combined effective exposure time of 17069 s (4.74 hrs).

We reduced the spectroscopic data using the *JWST* Calibration Pipeline[32] (H. Bushouse et al. 2025) version 1.17.1 and CRDS version `1350.pmap`. We largely used the default configuration for the pipeline with a few notable exceptions. First, we enabled the `clean_flicker_noise` step (using the "median" method[33]) in the `calwebb_detector1` stage to remove the effects of 1/f noise in the count rate maps. We also employed a modified flat-field file in the `calwebb_spec2` stage (see P. Arrabal Haro et al. 2023, for details). Beyond these changes, we ran the `calwebb_spec3` stage using the CRDS defaults to produce a final 2D spectrum (see Figure 1, middle panel).

We next used a custom optimal extraction (K. Horne 1986) to best detect and extract the signal from the source in the 2D spectrum to produce a 1D spectrum. Finally, we calibrated this 1D spectrum to the

[32] https://github.com/spacetelescope/jwst

[33] Based on image1overf.py https://github.com/chriswillott/jwst

JWST/NIRCam photometry provided by the PRIMER survey (§2.2) by computing the total flux in the spectrum within each of the F150W, F200W, F277W, F356W, and F444W NIRCam passbands. Specifically, we compared these measured fluxes to the photometric measurements of the object from NIRCam and fitted a third-order Chebyshev polynomial to the ratios between the spectrum and the photometry (as in `BAGPIPES`; A. C. Carnall et al. 2018). This correction peaks at a factor of ∼0.9 in F150W and quickly flattens to ∼0.7 from F200W through F444W. We then multiplied the 1D spectrum by the resulting fitted correction curve to produce our final calibrated 1D spectrum (see Figure 1, lower panel). This calibration is necessary to correct for the effects of NIRSpec path-loss and automated corrections applied in the *JWST* Calibration Pipeline that are not tied to NIRCam data.

2.2. *NIRCam Photometry*

The analysis in this paper makes use of *JWST*/NIRCam photometry in the PRIMER-COSMOS field. This imaging is an internal reduction from the PRIMER team (internal version 1.0). The PRIMER imaging data were reduced using the PRIMER Enhanced NIRCam Image Processing Library (PENCIL; Magee et al., in preparation, Dunlop et al., in preparation) software.

The photometry was measured via a similar process as in S. L. Finkelstein et al. (2024). Briefly, for each band of imaging, this methodology PSF-matches images (using empirical PSFs) with smaller PSFs than F277W to that band, and derives correction factors for images with larger PSFs (via PSF-matching F277W to a given larger PSF). Kron apertures are used to measure colors to optimize signal-to-noise for high-redshift galaxies. Total fluxes are estimated by deriving an aperture correction in the F277W band as the ratio between the flux in the larger Kron aperture and the custom smaller aperture, with a residual aperture correction (typically <10%) derived via source-injection simulations. We show cutouts of the imaging of CAPERS-LRD-z9 and list the measured magnitudes in Figure 1 (upper panel).

2.3. *MIRI Photometry*

We searched the Barbara A. Mikulski Archive for Space Telescopes (MAST) for MIRI data at the position of CAPERS-LRD-z9. It was located in a gap of the PRIMER observations but was covered by the COSMOS-3D survey (PID 5893) on 2025 April 20. Raw data were downloaded from MAST and reduced with the Rainbow MIRI software (P. G. Pérez-González et al. 2024) using the *JWST* Calibration Pipeline version v1.18.0, reference files in `jwst_1364.pmap`. The Rainbow software implements a super-background strategy to remove and homogenize the background, improving the detectability of faint sources. We refer the reader to P. G. Pérez-González et al. (2024) and G. Östlin et al. (2025) for details on the method, and for a discussion of improvements compared to ETC estimations. COSMOS-3D obtained data in the F1000W and F2100W filters, with exposure times of 927 s and 1848 s, respectively. The average 5σ detection limits for point-like sources measured in a circular aperture of radius $r = 0.3, 0.7''$ for F1000W, F2100W are 24.8, 22.8 mag, respectively (calculated with the method described below).

We measured photometry in the two MIRI bands assuming a point-like nature and applying aperture corrections based on the empirical PSFs provided by the *JWST* Calibration Pipeline. We used several circular apertures in each band. We selected radii ranging from $0.2''$ to $0.5''$ for F1000W and $0.4''$ to $1.0''$ for F2100W, the ranges of apertures sizes chosen to be able to detect faint sources and limited to maximum/minimum aperture losses of 50/25% for point-like sources. The background was measured in a $r = 10''$ circular region around the source. For the background noise (used to get photometric uncertainties and the 5σ detection limits quoted above), following the method explained in P. G. Pérez-González et al. (2023, based on P. G. Pérez-González et al. 2008), we selected random non-contiguous pixels (separated by more than 3 pixels) to avoid the effects of noise correlation (i.e., an underestimation of the rms) introduced by the drizzling method when mosaicking the data.

For F1000W, we obtained consistent photometric measurements (within errors) with all apertures, the measurements ranging from 24.90 ± 0.29 mag for $r = 0.2''$ to 25.63 ± 0.59 mag for $r = 0.5''$. The final magnitude used in the rest of the paper, the one with maximum SNR obtained with $r = 0.3''$ (aperture correction 0.60 ± 0.03 mag, the errors accounting for a 1 pixel centering error), is 25.02 ± 0.26 mag.

For F2100W, we obtained negative fluxes or S/N < 2 measurements for all apertures, so we conclude a non-detection in this band, and assume the 5σ upper limit quoted above of 22.8 mag (corresponding to an aperture of radius $r = 0.9''$, where the encircled energy is $\sim 70\%$).

3. DATA ANALYSIS

3.1. *Spectroscopic Redshift*

The CAPERS team is using a combination of software tools, interactive inspection, and manual vetting to measure redshifts from the NIRSpec spectra; the full methodology will be detailed in a forthcoming publica-

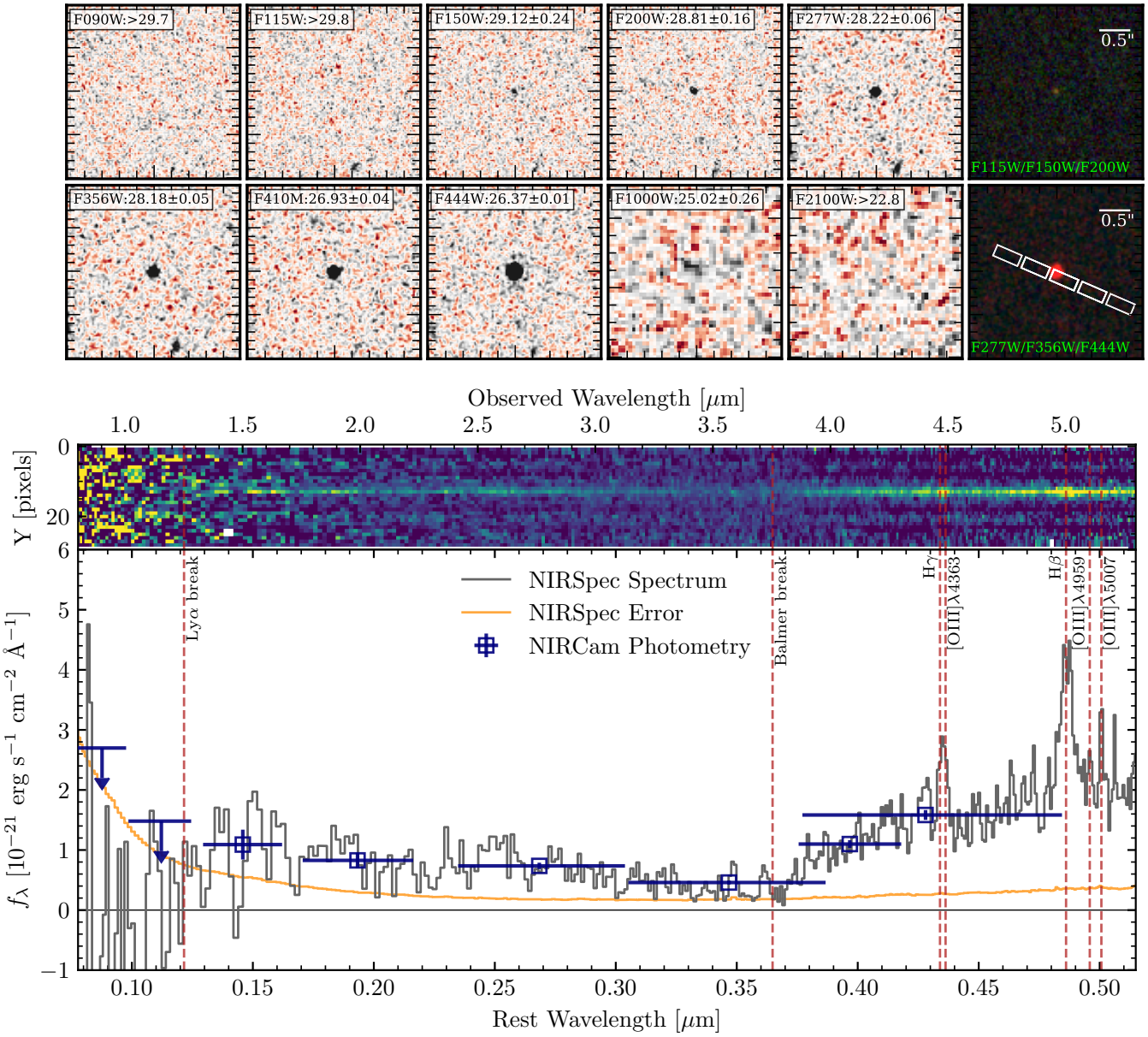

Figure 1. Top: $5'' \times 5''$ NIRCam and MIRI cutouts of CAPERS-LRD-z9 in the PRIMER-COSMOS NIRCam and COSMOS-3D MIRI images. We also show RGB images generated for both the short wavelength (SW) and long wavelength (LW) NIRCam detectors. We overplot the NIRSpec MSA slitlet. Bottom: We plot the 2D and 1D photometrically calibrated spectra of CAPERS-LRD-z9 in f_λ. We mark strongly detected emission features with red dashed lines and overplot the NIRCam photometry with blue squares. Despite being near the corner of the central shutter in the slitlet, CAPERS-LRD-z9 exhibits a detectable Lyα break, a strong Balmer break, and clear rest-optical emission line detections–including broadened Hβ and Hγ, and narrow [O III]$\lambda\lambda$4959, 5007. The combination of narrow forbidden lines and a broad Hβ clearly indicates that CAPERS-LRD-z9 is a BLAGN at $z = 9.288$.

tion. For CAPERS-LRD-z9, we derive the initial spectroscopic redshift using a modified version of `msaexp`[34] (G. Brammer 2022; V. Kokorev et al. 2024b). Key modifications include the ability to vary the velocity width and to model individual lines with multiple components (e.g., narrow and broad).

We use `msaexp` to fit the continuum with cubic splines and emission lines with Gaussian profiles. For this step, we adopt `nsplines=20`, leaving the position, amplitude, and width of emission lines as free parameters. The FWHM is allowed to vary between 150–800 km/s for narrow components and 800–5000 km/s for broad ones. Uncertainties are estimated via MCMC, using resampling of the covariance matrix. All fits are performed on spectra corrected to match the photometry. To account for the wavelength-dependent resolution of PRISM, the model grid is initially generated on an oversampled wavelength axis and then convolved with the instrument dispersion curve.

With this automated multi-line fitting approach we derive an initial $z_{\rm spec} = 9.2880 \pm 0.065$ and a number of interesting features. Broad components in excess of $\sim$ 3000 km/s are required to adequately model both the Hγ and $H\beta$ emission, while the adjacent lines in the [O III]$\lambda\lambda$4959, 5007 doublet remain narrow ($\sim$ 200 km/s). The presence of broad permitted (e.g. Balmer series of hydrogen) and narrower (semi-) forbidden lines like [O III], gives us a first hint that an accreting supermassive black hole is present in CAPERS-LRD-z9, typical of other spectroscopic investigations of LRDs with *JWST* (e.g. J. Matthee et al. 2024; D. D. Kocevski et al. 2025; A. J. Taylor et al. 2024).

We note that this redshift-fitting routine is not always capable of accurately modeling all spectral features. While it performs well for most narrow and broad emission lines and is efficient for processing large spectral samples, its reliability decreases in the presence of complex line blends, uncommon line ratios, low signal-to-noise regions, or noisy continua. Accurate identification of key features, such as broad lines, is essential for robust classification of the object, especially when using the PRISM data. Therefore, in subsequent sections, we adopt a more refined fitting procedure for select regions of the spectrum.

3.2. *Line Fitting*

The spectrum of our object presented in Figure 1 coupled with our initial `msaexp` fit hint at the presence of broad component in both Hγ and Hβ emission lines, in contrast to the narrower profiles of the adjacent [O III]$\lambda\lambda$4959,5007 Å doublet. Further, the Hβ line appears to be double peaked, which hints at an underlying absorption component. To evaluate the potential significance of these features we perform a more detailed line fitting to the Hγ+[O III]λ4363 and Hβ+[O III]$\lambda\lambda$4959, 5007 line complexes. The redder end of the PRISM where the Hβ+[O III]$\lambda\lambda$4959, 5007 is located has a higher spectral resolution, and this line complex is not blended, therefore we fit that region first. We assume that the lines in the [O III] doublet are both narrow, while the Hβ consists of a narrow, a broad and an absorption component. In our fitting, we assume that the velocity width of the narrow component for all three lines is the same, and we fix the ratio [O III]λ5007/[O III]λ4959 = 2.98 (P. J. Storey & C. J. Zeippen 2000). Velocities of the narrow, broad and absorption components are allowed to vary between $50-800$, $1000-5000$ and $50-1000$ km s^{-1}, respectively. We fix the redshift (and thus the line centers of the narrow lines using the vacuum wavelengths from P. A. M. van Hoof 2018), however we allow for small ($\sim \pm 500$ km/s) offsets in the absorption component and broad component of Hβ (relative to the narrow [O III]) to allow for kinematic motion of gas. We model the local continuum with a first-order polynomial.

We initialize the fit by first creating a set of models on the over-sampled wavelength grid. To mimic the variable resolution of the PRISM, we interpolate our model onto a variable step grid, while making sure that the total integrated flux is preserved. Early NIRSpec/MSA results (A. G. de Graaff et al. 2023) have shown that the spectral resolution of a point-like source falling within a slitlet is higher, compared to a uniformly illuminated slit, sometimes up to a factor of two. We therefore conservatively increase the nominal spectral resolution by a factor of 1.7. To take into account the effects of the line spread function, we additionally convolve our model with Gaussians of variable resolution (A. G. de Graaff et al. 2023; Y. Isobe et al. 2023). We then optimize this fit via MCMC with the `emcee` (D. Foreman-Mackey et al. 2013) package for `python`.

From our fit we securely (combined S/N $\approx$ 4.2) confirm the presence of the [O III]$\lambda\lambda$4959, 5007 doublet at a redshift $z = 9.288 \pm 0.003$. We adopt this redshift for all subsequent calculations. We also detect a distinct broad component in Hβ at S/N $\approx$ 10, with an intrinsic FWHM = 3521 ± 502 km s^{-1} and a tenuous slight redward velocity offset from the systemic redshift of 134 ± 164 km s^{-1}. The width of the narrow lines is poorly constrained due to the low resolution of the PRISM, although we report a posterior value of FWHM = 483 ± 225 km s^{-1}. The narrow component of

[34] https://github.com/VasilyKokorev/msaexp_OLF

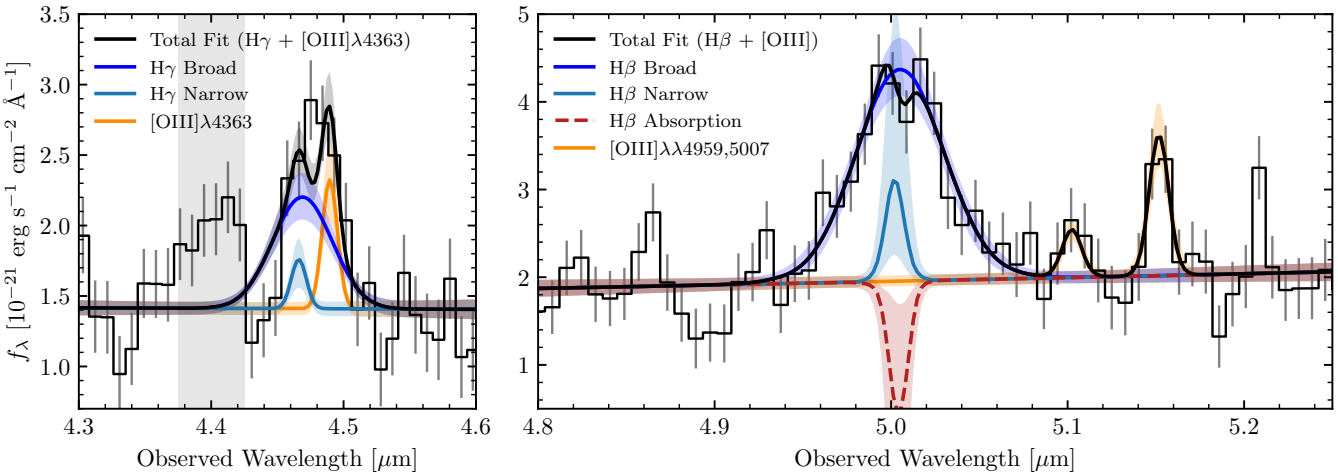

Figure 2. The observed NIRSpec/PRISM spectrum of CAPERS-LRD-z9 is shown as the fine black curve with uncertainties in gray. Left: Line fits and 1σ uncertainties on Hγ (blue curves and shaded regions), [O III]λ4363 (orange curve and shaded region) and the combined fit (thich black curve and shaded region). We de-blend these lines using the high confidence line widths and redshift solution measured from Hβ+[O III]$\lambda\lambda$4959, 5007. We show the region of masked spurious pixels with gray shading. Right: Line fits to Hβ+[O III]$\lambda\lambda$4959, 5007. A broad (FWHM= 3521 ± 502 km s^{-1}, blue curve) component is clearly necessary to reproduce the Hβ. We also fit narrow emission (light blue) and absorption (dashed red) components to Hβ to better model the double peak structure of the line, though their fluxes are degenerate at PRISM resolution. The [O III]$\lambda\lambda$4959, 5007 doublet is also detected at S/N $\sim$ 4. The combination of narrow [O III]$\lambda\lambda$4959, 5007 and broad Hβ are clear indicators of a broad-line AGN.

Hβ does not appear statistically significant (S/N $\approx$ 0.8). Additionally, while including the Hβ absorption component results in a visually better fit to the double peaked $H\beta$ line with a line width of FWHM = 413 ± 255 km s^{-1}, and slight redward offset of 84 ± 126 km s^{-1} this component is also statistically insignificant with (S/N $\approx$ 1.1) and highly degenerate with the narrow Hβ component. These statistical non-detections may be expected at the resolution of the PRISM, but as they are physically motivated, we include them in the model regardless to better sample their covariance with the more significant model components.

The situation with Hγ+[O III]λ4363 is more complex, as these lines are blended at the PRISM resolution. We can however use the prior information obtained from the Hβ+[O III]$\lambda\lambda$4959, 5007 complex and attempt to adequately separate the two lines. We fix the narrow and broad line widths, broad velocity offset, and redshift to the result we obtained from the Hβ+[O III]$\lambda\lambda$4959, 5007 fit, and only fit the integrated fluxes of narrow+broad Hγ, narrow [O III]λ4363, and a first-order polynomial continuum. Finally, the flux ratio of the narrow Hγ to narrow Hβ is not allowed to exceed 0.47, as set by Case B recombination (D. E. Osterbrock 1989). This fit is further complicated by six consecutive pixels at 4.375–4.425μm that show flux above the level of the nearby continuum. While these pixels are detected at the 1–3σ level above the continuum, they correspond to no known emission line. Therefore, we conservatively mask out this spurious feature. We once again forward model the effects of the PRISM resolution and fit the Hγ+[O III]λ4363 line complex with MCMC. Similarly to Hβ, we could not derive a significant flux for a narrow Hγ (S/N $\approx$ 2), however, we detect and partially deblend a broad Hγ component at S/N $\approx$ 4.8 and [O III]λ4363 at S/N $\approx$ 3.1. We note that the blue wing of the broad Hγ line appears higher than the data. This may indicate that the masked spurious feature is affecting these pixels, or that the Hγ broad line width is narrower than that of Hβ, as has been seen in low-redshift quasars (e.g. M. C. Bentz et al. 2023). As our analyses are not dependent on the Hγ width, this uncertainty does not affect our interpretation of this object. We present various measured and derived properties of CAPERS-LRD-z9 in Table 1 and show our best-fit models to both line complexes in Figure 2.

3.3. *Morphology and Size Measurements*

To determine if any of the emission from CAPERS-LRD-z9 might originate from an extended stellar population, we use the `GALFIT` software (C. Y. Peng et al. 2002) to model the galaxy as a point source in several NIRCam bands, to search for signs of an underlying galaxy in the residual image. For this modeling, we provide `GALFIT` with empirical PSFs constructed from the PRIMER-COSMOS mosaic and noise images that account for both the intrinsic image noise (e.g.,

Table 1. Properties of CAPERS-LRD-z9

Property	Value
R.A.	150.1362532 deg
Decl.	2.3080298 deg
Redshift (z)	9.288 ± 0.003
Hγ flux (narrow)	< 7.1
Hγ flux (broad)	45.9 ± 9.5
[O III]λ4363 flux	13.0 ± 4.2
Hβ flux (narrow)‡	< 62.7
Hβ flux (broad)	140 ± 14.6
Hβ flux (absorption)	> -69.1
H$\beta_{\rm broad}$ FWHM	3521 ± 502 km s^{-1}
H$\beta_{\rm abs}$ FWHM	282 ± 159 km s^{-1}
H$\beta_{\rm broad}$ offset	134 ± 164 km s^{-1}
H$\beta_{\rm abs}$ offset	84 ± 126 km s^{-1}
[O III]λ4959 flux	7.2 ± 3.5
[O III]λ5007 flux	22.2 ± 5.3
[O III]λ5007 FWHM	483 ± 225 km s^{-1}
$M_{1500\text{Å}}$	-18.2 ± 0.2 mag
$\beta_{\rm UV}$	$-0.99^{+0.14}_{-0.13}$
$\log(M_{\rm BH}/M_\odot)$ (canonical)	7.58 ± 0.15
$\log(M_{\rm BH}/M_\odot)$ (systematic bounds)	6.65–8.50
$A_{\rm V,BLR}$	$1.9^{+1.3}_{-1.2}$
$\log(M_*/M_\odot)$	< 9.0
$M_{\rm BH}/M_*$ (canonical)	$> 4.5\%$
$M_{\rm BH}/M_*$ (systematic bounds)	$> 46\%, > 0.5\%$
Balmer Break: $(f_{\nu,4050\text{Å}}/f_{\nu,3670\text{Å}})$	$4.35^{+0.93}_{-0.67}$

NOTE—All line fluxes are given in units of 10^{-20} erg s^{-1} cm^{-2}. Lines fit at S/N$\leq$2 are listed as 2σ (upper/lower) limits on their fluxes. We define a "canonical" $\log(M_{BH}/M_\odot)$ and uncertainties as only those errors propagating from the measured broad-line properties and the empirical uncertainties given in (J. E. Greene & L. C. Ho 2005) without correcting for dust. We further provide upper and lower bounds on $\log(M_{\rm BH}/M_\odot)$ to account for systematic uncertainties in the measurement methods (see §4.2 for details).

background and readout noise) and added Poisson noise due to the objects themselves. We show the results of this morphological modeling in Figure 3 for F200W and F444W. We see no signs of any extended structure, indicating that the source is unresolved or the surface brightness of the resolved component is too low for detection with the sensitivity of our image. We estimate an upper limit on the size of the host to be $r_h < 0\farcs04$ and $0\farcs08$ in F200W and F444W, respectively, which correspond to physical sizes of $\lesssim 175$ pc and $\lesssim 350$ pc.

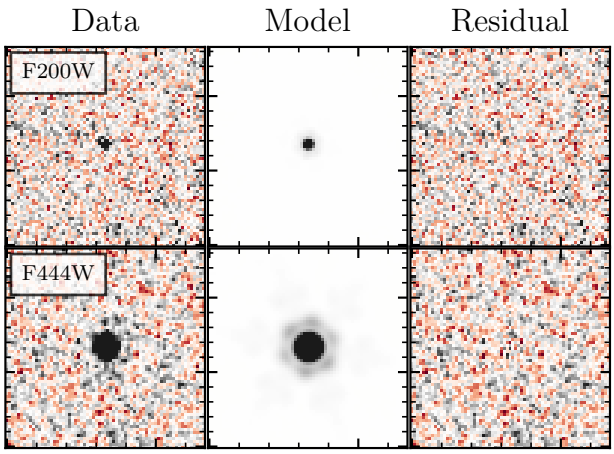

Figure 3. Results of two-dimensional surface brightness profile fitting. We show $2'' \times 2''$ cutouts in F200W and F444W around CAPERS-LRD-z9 in the left column. Our best-fit, point-source models in each band are shown in the middle column, while the residuals (data-model) are shown in the rightmost column. CAPERS-LRD-z9 is unresolved in all bands, with $r_h < 0\farcs04$ and $0\farcs08$ in F200W and F444W, respectively, corresponding to respective physical sizes of $\lesssim 175$ pc and $\lesssim 350$ pc.

3.4. *Spectrophotometric Fitting*

We model the SED of CAPERS-LRD-z9 as a composite galaxy+AGN, similar to previous work on LRDs with Balmer breaks (e.g. B. Wang et al. 2024b; I. Labbe et al. 2024). However, here we model the Balmer break as part of the AGN continuum (rather than old stars), driven by absorption from a shell of dense gas around the accretion disk/broad line region (BLR; e.g. K. Inayoshi & R. Maiolino 2025; X. Ji et al. 2025; R. P. Naidu et al. 2025). We explored modeling the spectrum using only a stellar component, with flexible non-paramteric star-formation history (SFH) driving the strong Balmer break with an old stellar population ($>$ 300 Myr). Comparing the fluxes on either side of the break (in 100 Å-wide windows centered at 3670 and 4050 Å), our best-fit stellar-only model has a break strength of ~ 2.8. This is insufficient to match the strength of the break in CAPERS-LRD-z9 (which we measure as $f_{\nu,4050\text{Å}}/f_{\nu,3670\text{Å}} = 4.35^{+0.93}_{-0.67}$), similar to other recently discovered LRDs with even more extreme Balmer breaks (MoM-150135; $7.7^{+2.3}_{-1.4}$; R. P. Naidu et al. 2025, RUBIES-UDS-154183; $6.9^{+2.8}_{-1.5}$; A. de Graaff et al. 2025). The stellar-only model is overall a poor fit to the data, with a Bayesian Information Criterion (BIC) difference from our fiducial model (described below) of ΔBIC > 80. This, combined with the significant detection of broad Hβ, drives our assumption that the rest-frame optical is dominated by the AGN, enshrouded in dense gas.

Table 2. CLOUDY parameter grid & fitted values

Parameter	Grid Values	Fitted Value
$\log T_{\rm BB}/{\rm K}$	4, 4.7, 5, 5.7	5.0
$\alpha_{\rm OX}$	−2.5, −2.0, −1.5	−1.5
$\alpha_{\rm UV}$	−0.1	...
$\alpha_{\rm X}$	−0.5	...
$\log n_H/{\rm cm}^{-3}$	9, 9.5, 10, 10.5, 11, 11.5, 12	$9.9^{+0.2}_{-0.2}$
$v_{\rm turb}/{\rm km\,s}^{-1}$	100, 200, 300, 400, 500	320^{+80}_{-60}
[Fe/H]	−2	...
$\log U$	−3.5, −3, −2.5, −1.5, −0.5	−1.5
$\log N_H/{\rm cm}^{-2}$	21, 22, 23, 24, 25, 26	$> 25.9^{\dagger}$
C_f	0–1	$0.12^{+0.01}_{-0.01}$
A_V	0–3 (SMC law)	$0.53^{+0.09}_{-0.08}$

NOTE—The first four parameters describe the incident continuum spectrum where $T_{\rm BB}$ is the 'Big Bump' temperature, $\alpha_{\rm OX}$ is the optical to X-ray index, $\alpha_{\rm UV}$ is the power-law UV slope and $\alpha_{\rm X}$ is the power-law X-ray slope. The incident continuum is passed through dense gas defined by the gas density (n_H), metallicity ([Fe/H]) and turbulent velocity ($v_{\rm turb}$). The level of irradiation at the face of the cloud is set by the ionization parameter ($\log U$) and the CLOUDY calculations are stopped at a range of line-of-sight column densities (N_H).
† We provide the 1σ lower limit for the column density as our posterior is limited by the edge of the CLOUDY grid.

We therefore pursue a more complex modeling, first using the CLOUDY photoionization code (version 23.01; M. Chatzikos et al. 2023) to generate a large grid of AGN model SEDs, varying both the intrinsic AGN accretion disk SED and the gas conditions around the source. We follow the framework described in K. Inayoshi & R. Maiolino (2025) and R. P. Naidu et al. (2025) and model the intrinsic AGN accretion disk SED as a series of power laws combined with a 'Big Bump' temperature.[35] This continuum is passed through a shell of gas surrounding the central source which is defined in terms of its density, metallicity, and turbulent velocity. The turbulence is required to reproduce the break shape; without it, the break is very sharp at $\lambda = 3650$ Å. We vary the ionization parameter which sets the ratio of H-ionizing photons to gas densities at the illuminated face of the gas cloud. When all other parameters are fixed, varying the ionization parameter is equivalent to varying the distance between the central source and the gas shell. We stop the calculation at a set of fixed line of sight column densities through the gas cloud. The full grid of CLOUDY model parameters is provided in Table 2.

In order to conduct joint inference on the AGN and galaxy parameters, we assemble and fit the full SED model using a modified version of bagpipes (A. C. Carnall et al. 2018), a Bayesian SED modeling code. bagpipes requires models with a continuous parameter space, rather than discrete points in a grid; we include a custom module to interpolate over the CLOUDY grid (consisting of both the continuum and emission lines of the AGN processed through the dense gas shell).

However, in an effort to reduce the dimensionality of the problem, prior to fitting with bagpipes we first perform a simple χ^2 minimization routine over the CLOUDY grid to identify and fix best-fit values of several grid parameters. Here, we fit only to the PRISM spectrum redward of the Balmer break, and include several post-processing steps, including broadening of the AGN emission lines, a variable covering fraction of the BLR clouds, and dust attenuation following an SMC law (K. D. Gordon et al. 2003). Fitting to our grid, we find the best-fit model has $\log T_{\rm BB}/K = 5$, $\alpha_{\rm OX} = -1.5$, $\log n_H/{\rm cm}^{-3} = 9.5$, $v_{\rm turb} = 100$ km s^{-1}, $\log U = -1.5$, and $\log N_H/{\rm cm}^{-2} = 26$.

In the subsequent modified bagpipes fit, we then fix $T_{\rm BB}$, $\alpha_{\rm OX}$, and $\log U$ at their best-fit values and interpolate over the density $\log n_H$, column density $\log N_H$, and turbulent velocity $v_{\rm turb}$. These parameters predominantly impact the strength and shape of the Balmer break (see X. Ji et al. 2025), and are therefore important to model flexibly to optimize the fit. We adopt uniform priors for each parameter, and again include a broadening of the AGN emission lines, a variable covering fraction of the BLR clouds (C_f), and dust attenuation (A_V; SMC law); we note that we explored allowing the attenuation curve slope to vary, but find no need for an extremely steep dust law (in contrast to A. de Graaff et al. 2025).

For the galaxy model, we use the BPASS v2.2.1 stellar templates (E. R. Stanway & J. J. Eldridge 2018) and a flexible star-formation history via the "bursty continuity" parametrization described in S. Tacchella et al. (2022). We use five fixed age bins with edges at 0, 10, 30, 100, 200, and 300 Myr and a log-uniform prior on the stellar metallicity from 0.1% to 100% solar. We include nebular emission, varying $\log U$ from −4 to −1, and dust attenuation (SMC law). Note that the dust attenuation is fit separately for the stars and AGN.

The final model is the combination of the stellar and AGN components, with the normalization of the latter fit as a free parameter. The model spectrum is con-

[35] This AGN continuum model is described in Section 6.2 of the HAZY1 CLOUDY documentation (version 23.01).

volved with the PRISM resolution curve and the joint model is fit to both the NIRSpec spectrum and the NIRCam+MIRI photometry. We note that we mask the [O III]$\lambda\lambda$4959,5007 doublet when fitting the spectrum, as these lines are likely coming from the NLR (see §4.4), which is not considered in our `CLOUDY` modeling of the BLR and nearby gas or our stellar model. We additionally mask the region around H_∞ (3630–3690 Å), where the `CLOUDY` modeling yields artifacts due to the finite number of resolved energy levels (K. Inayoshi & R. Maiolino 2025; X. Ji et al. 2025). The resulting best-fit model is shown in Figure 4, and the results from the spectrophotometric modeling are discussed in Sections 4.3 and 4.4.

4. RESULTS

4.1. *Dust Attenuation*

The ratio of observed fluxes from the Balmer series lines provides a measure of dust attenuation. Here we use the observed Hβ/Hγ ratio. As illustrated in Figure 2, the Hγ line is blended with [O III]λ4363. While we use priors based on the Hβ+[O III]$\lambda\lambda$4959, 5007 line widths to de-blend these lines, the per-pixel S/N for Hγ is not sufficient for a double-component fit. Since we cannot isolate the narrow component of Hγ or Hβ, we compute a Balmer decrement for the BLR solely based on the ratio of Hβ and Hγ broad components' fluxes, ensuring flux integration across comparable velocity ranges. This yields $\mathrm{H}\beta/\mathrm{H}\gamma = 3.5^{+1.7}_{-0.9}$.

To calculate A_V, we apply the Small Magellanic Cloud (SMC) reddening law (K. D. Gordon et al. 2003), which has been found to match well the dust attenuation in high-z galaxies (P. L. Capak et al. 2015; N. A. Reddy et al. 2015, 2018) and reddened quasars (e.g. see A. M. Hopkins 2004). Assuming Case B recombination, the intrinsic line ratio would be $(\mathrm{H}\beta/\mathrm{H}\gamma)_\mathrm{int}$=2.14 (D. E. Osterbrock 1989). Our observed ratio suggests significant attenuation; we estimate $A_\mathrm{V,BLR} = 1.9^{+1.3}_{-1.2}$ (where our precision is limited primarily by the S/N $\approx$ 4 detection of broad Hγ). We note that while Case B recombination may not be a sound assumption for collisionally excited gas, this nonetheless provides an estimate of the reddening of the BLR.

4.2. *Black Hole Mass*

Black hole mass estimation from broad emission lines relies on two fundamental assumptions: the broad-line emitting gas is virialized and dominated by the gravitational potential of the central black hole, and a "radius–luminosity" relationship exists between the broad-line orbital radius and the AGN luminosity (in Equation 1, the Hβ broad-line luminosity). These assumptions have generally been validated for low-redshift AGN (e.g. M. C. Bentz et al. 2006; E. M. Cackett et al. 2021) but their applicability to the broader AGN population is less certain.

In the specific case of CAPERS-LRD-z9, the broad and symmetric Hβ line profile is consistent with the basic virial assumption for kinematics dominated by gas orbits around a massive black hole, in contrast to the asymmetric broad-line profiles commonly observed in quasars with significant non-virial kinematics (e.g. V. U et al. 2022; L. B. Fries et al. 2024). The reliability of the radius–luminosity assumption is more difficult to assess. Compared to the radius–luminosity relation measured for Seyfert 1 AGN that was used to calibrate single-epoch masses, recent studies have shown that luminous and rapidly accreting quasars have smaller BLR sizes (P. Du et al. 2016; G. Fonseca Alvarez et al. 2020), which leads to smaller black hole masses. The empirical radius–luminosity relation is generally assumed to be caused by a photoionization-bounded broad-line region (e.g. K. T. Korista & M. R. Goad 2004), and the unusual SED shape of LRDs like CAPERS-LRD-z9 could result in a significantly different BLR structure compared to other quasars. Elevated Eddington ratios also affect the radius–luminosity relation and may also result in the overestimation of black hole masses by as much as an order of magnitude (e.g.. P. Du et al. 2016; A. Lupi et al. 2024). We ultimately use the canonical relationship for low-redshift AGN of Equation 1 to estimate a mass for CAPERS-LRD-z9, while acknowledging that significant work must be done to better understand the applicability of mass estimates for high-redshift LRDs.

To compute the canonical black hole mass, we use Equation 10 from J. E. Greene & L. C. Ho (2005), where $L_{\mathrm{H}\beta}$ and $\mathrm{FWHM}_{\mathrm{H}\beta}$ are the luminosity and FWHM of the broad component of Hβ, respectively.

$$\begin{aligned} M_\mathrm{BH} &= (2.4 \pm 0.3) \\ &\quad \times 10^6 \left(\frac{L_{\mathrm{H}\beta}}{10^{42}\ \mathrm{erg\ s^{-1}}}\right)^{0.59\pm0.06} \\ &\quad \times \left(\frac{\mathrm{FWHM}_{\mathrm{H}\beta}}{10^3\ \mathrm{km\ s^{-1}}}\right)^2 M_\odot \end{aligned} \tag{1}$$

Propagating the uncertainties on the calibration coefficients given in the empirical relation and the uncertainties on our line flux and FWHM, we derive a black hole mass for CAPERS-LRD-z9 of $\log(M_\mathrm{BH}/M_\odot) = 7.58 \pm 0.15$. We note that additional systematic uncertainties from applying the J. E. Greene & L. C. Ho (2005) relations at high redshift may be as high as 0.5-0.7 dex (G. Fonseca Alvarez et al. 2020; R. Abuter et al. 2024).

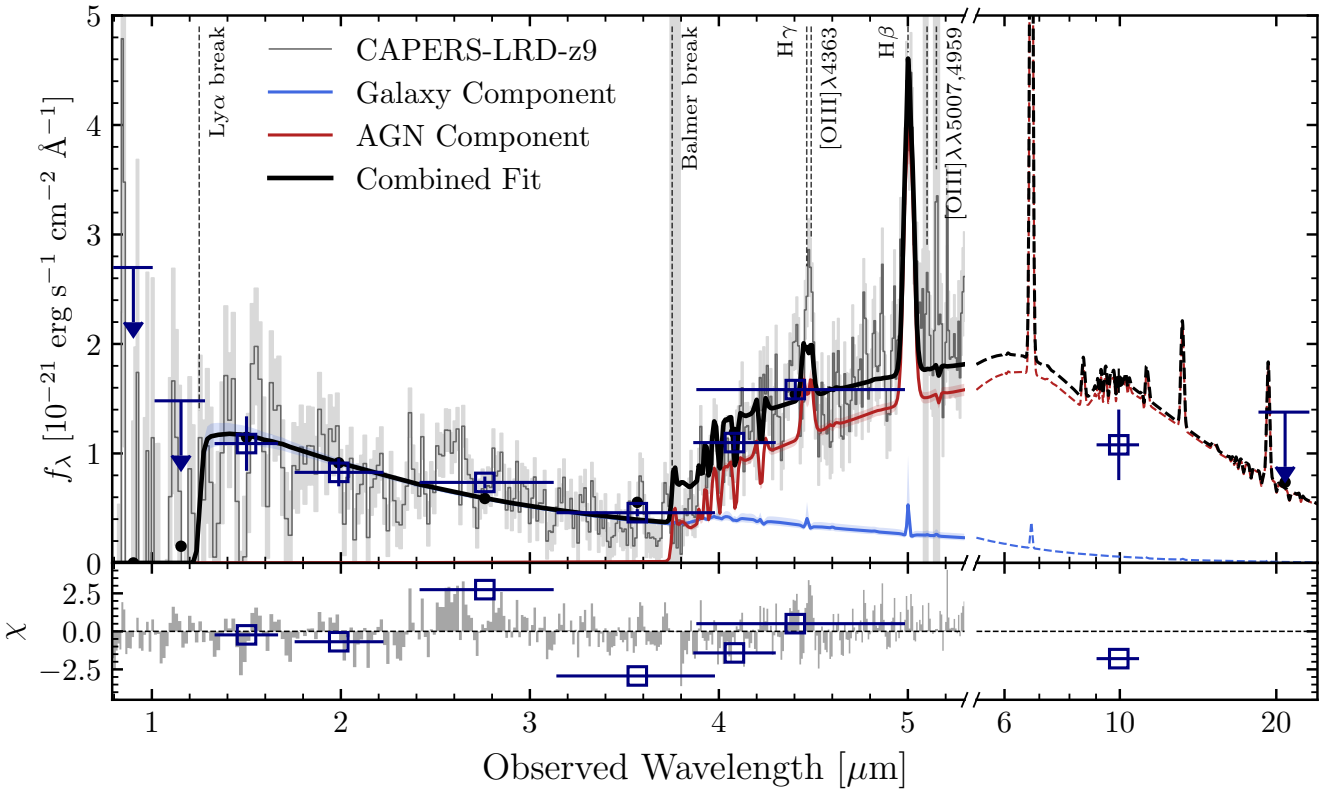

Figure 4. Spectrum and 1σ errors of CAPERS-LRD-z9 (gray curve, light gray shading), the best fit host galaxy component (blue and dashed blue curves), the best fit dense-gas enshrouded AGN component (red and dashed red curves), combined host+AGN fit (black and dashed black curves), photometry data (dark blue squares and upper limits), and best-fit model photometry (black points) in the upper panel. The lower panel shows the χ residuals of the fit for the spectrum (gray curve) and photometry (dark blue squares). Note that neither the `BAGPIPES` stellar model nor the `CLOUDY` AGN model can match the strong [O III]λ4363 emission.

To best capture these true systematic uncertainties and account for the limitations of our PRISM data, we next compute strong upper and lower limits on $\log(M_{\rm BH}/M_\odot)$. First, we derive an upper bound by correcting our canonical measurement for dust attenuation. By adopting the estimated reddening of $A_{\rm V,BLR} = 1.9^{+1.3}_{-1.2}$ (computed above), we derive a higher black hole mass of $\log(M_{\rm BH}/M_\odot) = 8.10 \pm 0.40$. Using our $A_V \approx 0.53$ from our spectrophotometric fitting, we alternatively compute $\log(M_{\rm BH}/M_\odot) = 7.70 \pm 0.14$. Of these values, we adopt the 1σ upper limit on the Balmer decrement derived value ($\log(M_{\rm BH}/M_\odot) < 8.5$) as a strong upper limit on the black hole mass.

We also compute a lower limit on the black hole mass using the Hβ line luminosity and assuming that the AGN is accreting at the Eddington rate. For the purposes of computing a lower limit, we conservatively convert the Hβ luminosity to Hα luminosity assuming an unattenuated Case B ratio (Hα/Hβ=2.86; D. E. Osterbrock 1989), and use the bolometric correction from J. Stern & A. Laor (2012) to derive $\log(M_{\rm BH}/M_\odot) > 6.65$. This method has the benefit of being insensitive to the measured Hβ line-width. As such, it remains robust even if the Hβ line-width is significantly overestimated due to uncertainties in the effects of the NIRSpec/PRISM spectral resolution, or more exotic explanations for line broadening such as electron scattering (e.g., V. Rusakov et al. 2025).

When considering these upper and lower limits together, we compute systematic bounds on $\log(M_{\rm BH}/M_\odot)$ of 6.65–8.50. However, for ease of comparisons to other reported LRD black hole masses in the literature, we adopt our canonical measurement and its associated non-systemic error bounds for the remainder of this work (unless otherwise stated).

4.3. *Stellar Mass*

Properly estimating the stellar masses of LRDs has proven enormously difficult given the unclear origin of the "v-shaped" spectrum and degeneracies in decomposing the galaxy/AGN contribution (e.g. V. Kokorev et al. 2023; G. Barro et al. 2023; L. J. Furtak et al. 2024; B.

Wang et al. 2024a,b; H. B. Akins et al. 2024; I. Labbe et al. 2024). Here, we have assumed that the rest-UV is dominated by stars (with the rest-optical dominated by the AGN); however, we do not know this *a priori*. The stellar mass we derive is likely therefore an upper limit, as it is entirely possible that the UV is also AGN dominated (a possibility we discuss further in §5.3). The joint `bagpipes`+`CLOUDY` fitting described in §3.4 yields a host galaxy stellar mass of $\log(M_*/M_\odot) = 8.9^{+0.1}_{-0.1}$.

We note that stellar masses can be underestimated when derived from the UV alone, due to "outshining" from young O/B stars (see e.g. D. Narayanan et al. 2024). However, as there are no prominent emission features in the rest-UV of CAPERS-LRD-z9, and the rest-optical emission lines are accounted for via the AGN, the SFH model is not biased towards a young stellar population. In fact, the age-dust-metallicity degeneracy is accounted for in our posterior estimate. We explored including an additional burst of SF at $z = 20$, and found a consistent stellar mass with no meaningful improvement to the quality of the fit, showing that the observations do not allow for a significant mass in older stars to be present in this object.

From our computed stellar mass upper limit and our canonical measurement of $M_{\rm BH}$, we compute $M_{\rm BH}/M_* > 4.5\%$. Invoking our systematic lower and upper bounds for $M_{\rm BH}$, we alternatively compute $M_{\rm BH}/M_* > 0.5\%$ and $M_{\rm BH}/M_* > 46\%$, respectively. We plot this black hole to stellar mass ratio in Figure 5, along with a large body of literature samples (H. B. Akins et al. 2025a; L. J. Furtak et al. 2024; Y. Harikane et al. 2023; I. Juodžbalis et al. 2025; D. D. Kocevski et al. 2023, 2025; V. Kokorev et al. 2023, 2024a; R. Maiolino et al. 2024; I. Labbe et al. 2024; R. L. Larson et al. 2023; R. Tripodi et al. 2024; H. Übler et al. 2024; B. Wang et al. 2024a; M. Yue et al. 2024b). Figure 5 demonstrates the "over-massiveness" of CAPERS-LRD-z9 in the context of both literature samples of *JWST*-detected AGN (colored points) as well as the established mass ratio for local quasars of 0.1% (dashed black line). For comparison, we overlay the predicted evolution of $M_{\rm BH}/M_*$ ratios from $\sim 10^3$ early BH populations formed via two distinct seeding channels: heavy seeds (red contours) and light seeds (blue contours), based on the SP1 model presented in H. Hu et al. (2025).

The observed value of for CAPERS-LRD-z9 is broadly consistent with both scenarios, but the lower limit nature of this value may hint toward the heavey seed regime. We discuss possible explanations for this effect and its possible interplay with black hole seeding and growth in §5.1.

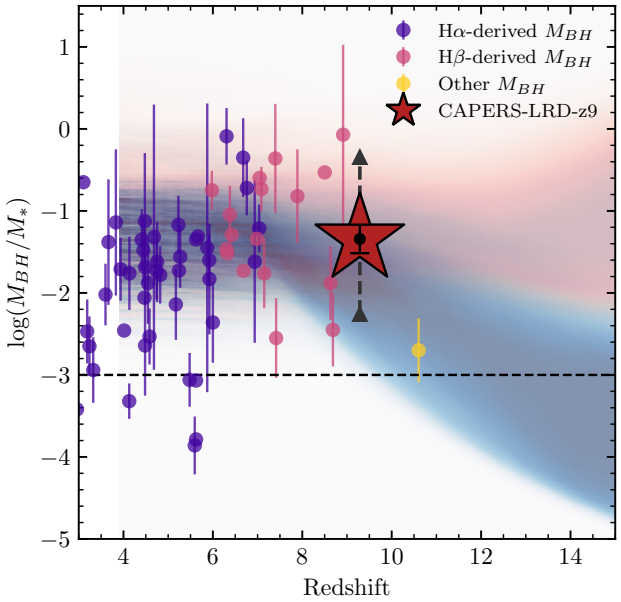

Figure 5. Black hole mass to stellar mass ratio $\log(M_{\rm BH}/M_*)$ as a function of redshift for CAPERS-LRD-z9 (red star) and a collection of literature *JWST*-detected AGN (H. B. Akins et al. 2025a; L. J. Furtak et al. 2024; Y. Harikane et al. 2023; I. Juodžbalis et al. 2025; D. D. Kocevski et al. 2023, 2025; V. Kokorev et al. 2023, 2024a; R. Maiolino et al. 2024; I. Labbe et al. 2024; R. L. Larson et al. 2023; R. Tripodi et al. 2024; H. Übler et al. 2024; B. Wang et al. 2024a; M. Yue et al. 2024b), showing the published errors, typically exclusive of systematic uncertainties. We divide the literature selected samples into those selected based on a broad Hα line (purple points), a broad Hβ line (pink points), and based on UV line or X-ray detections (yellow points). We plot the statistical errors on CAPERS-LRD-z9 as the black error bars, and we include a larger systematic range on $\log(M_{\rm BH}/M_*)$ based on the systematic limits on the black hole mass of CAPERS-LRD-z9 as a gray dashed line and upward pointing arrows. We stress that as our M_* measurement is an upper limit, all of our measurements of $M_{\rm BH}/M_*$ are lower limits. We plot the $M_{\rm BH}/M_* = 0.1\%$ value for local galaxies as a black dashed line. For comparison, we overlay the predicted evolution of $M_{\rm BH}/M_*$ ratios from early BH populations formed via two distinct seeding channels: heavy seeds (red shaded region) and light seeds (blue shaded region), based on the semi-analytical model presented in H. Hu et al. (2025). The population of *JWST*-detected AGN exhibits an apparent over-massiveness in this ratio compared to the local relation.

4.4. *Gas density & temperature*

Our best-fit AGN model has $\log n_H/{\rm cm}^{-3} \sim 9.9^{+0.2}_{-0.2}$, and $\log N_H/{\rm cm}^{-2} \gtrsim 26$. These are similar to the best-fitting parameters for MoM-150135 and RUBIES-UDS-154183 (R. P. Naidu et al. 2025; A. de Graaff et al. 2025), and suggest very extreme gas conditions in the BLR. To examine whether these conditions extend to

the narrow-line region (NLR), we look to the forbidden oxygen lines. We measure an extremely high ratio of [O III]λ4363/[O III]λ5007 (RO3) $= 0.58 \pm 0.23$ in CAPERS-LRD-z9. Though [O III]λ4363 is blended with Hγ at the PRISM resolution, our MCMC line fitting (described in §3.2) yields a significant [O III] detection (SNR ~ 3).

As the [O III]λ4363 and λ5007 lines arise from different upper energy levels, RO3 is commonly used as a temperature diagnostic. High RO3 traces high temperature regions of the ISM, and is found to be increasingly common in $z \gtrsim 8$ galaxies (J. Brinchmann 2023; H. Katz et al. 2023; F. Cullen et al. 2025). RO3 has also been used as an AGN diagnostic, particularly at high-redshift, where the canonical BPT diagram breaks down due to lower metallicity (B. E. Backhaus et al. 2023; G. Mazzolari et al. 2024). Here, the [O III]4363 line likely traces the NLR, or ISM gas heated by the AGN in addition to star-formation.

The ratio we observe for CAPERS-LRD-z9 (RO3 $\approx 0.58 \pm 0.23$) is particularly extreme, even compared to other $z > 7$ BLAGN (V. Kokorev et al. 2023; R. Tripodi et al. 2024; H. Übler et al. 2024). Such a high ratio is only possible at densities approaching (or exceeding) the critical density of [O III]λ5007 ($n_e \sim 7 \times 10^5\,\mathrm{cm}^{-3}$) where collisional de-excitation becomes important. The critical density for [O III]λ4363 is significantly higher ($\sim 10^8\,\mathrm{cm}^{-3}$). Using `pyneb` (V. Luridiana et al. 2015), we find that RO3 we measure corresponds to densities $\gtrsim 10^6$ cm^{-3}, even at very high temperatures $T_e \sim 10^5$ K. At lower temperatures ($T_e \sim 10^4$ K), the implied density is even high: $n_e \gtrsim 10^8$ cm^{-3}. This suggests that the NLR itself could be quite dense, corroborating the extreme densities inferred for the BLR.

5. DISCUSSION

5.1. *Implications for Black Hole Seeding and Growth*

We plot our canonical black hole mass for CAPERS-LRD-z9 in Figure 6, along with other notable $z > 6$ AGN from the literature. We also plot simple models of Eddington-limited black hole growth (with 10% radiative efficiency) for both stellar (light) seeds ($\sim 10^2 M_\odot$) and more massive heavy seeds ($\gtrsim 10^4 M_\odot$). The red shaded region corresponds to heavy seeds with formation redshifts of 25–15 that begin accreting at the Eddington limit immediately after formation. For the stellar remnant light seeds, we plot formation redshifts of 30-15 and require an additional 100 Myr to pass after the formation redshift before accretion begins due to progenitor gas heating by the pre-collapsed stars (e.g., J. L. Johnson & V. Bromm 2007). It is clear that CAPERS-LRD-z9's SMBH is too massive to form from a simple stellar remnant that grows at the Eddington rate, similar to what has been inferred for other recently discovered high-z AGN (e.g., R. L. Larson et al. 2023). However, a heavy seed growing at the Eddington rate can easily reproduce the observed BH mass, making it a plausible formation pathway. This scenario naturally establishes the over-massive $M_{\rm BH}/M_*$ configurations present at high-z, as shown in Figure 5 (see also the red shading representing the heavy-seed model prediction). Furthermore, the emerging SMBH demographics suggest that the BH-to-stellar mass ratio may bifurcate as we approach the highest redshifts, into a high- and low-$M_{\rm BH}/M_*$ branch. Such a bifurcation has been predicted for a hybrid seeding scenario, where the two branches are linked to heavy and light seeds, respectively (also see figure 3 in J. Jeon et al. 2025b).

A key uncertainty in all direct-collapse BH (DCBH) models is the choice of formation criteria, such as the required level of soft-UV (LW) background flux, or the critical metallicity above which gas cooling would become too efficient, resulting in cloud fragmentation which suppresses DCBH formation (e.g. V. Bromm & A. Loeb 2003; M. C. Begelman et al. 2006; K. Omukai et al. 2008; J. H. Wise et al. 2019). The value of these parameters is reflected in the resulting number densities of DCBH seeds and their descendants (e.g., A. Trinca et al. 2022; H. Hu et al. 2025; J. Jeon et al. 2025b). In turn, any firm limits on the DCBH abundance would significantly constrain the formation scenarios, as could be accomplished by linking the DCBH seeding pathway to a subset of the observed LRD population.

Some studies have suggested that the conditions required to form DCBH seeds are too rare for this channel to account for the majority of the SMBHs being detected by JWST (e.g., A. K. Bhowmick et al. 2024), whereas others argue for less restrictive conditions (e.g., S. Chon & K. Omukai 2025). However, observations suggest that ultradense star clusters may be common or even ubiquitous in high redshift galaxies (A. Adamo et al. 2024; L. Mowla et al. 2024; S. Fujimoto et al. 2024), providing a promising additional heavy seeding mechanism.

Furthermore, the heavy seed explanation is not the only way to produce CAPERS-LRD-z9's black hole mass by $z = 9.288$. Allowing (even mild) super-Eddington accretion with a stellar remnant seed can also reproduce the black hole mass of CAPERS-LRD-z9. For example, in Figure 6, we show that a $10^2 M_\odot$ stellar remnant formed at $z = 30$ growing at an average Eddington ratio of 1.85 after a 100 Myr delay in starting accretion can easily reproduce the BH mass of CAPERS-LRD-z9. In reality, we expect that super-Eddington accretion occurs in short bursts (e.g., E. Takeo et al. 2020; H. Suh

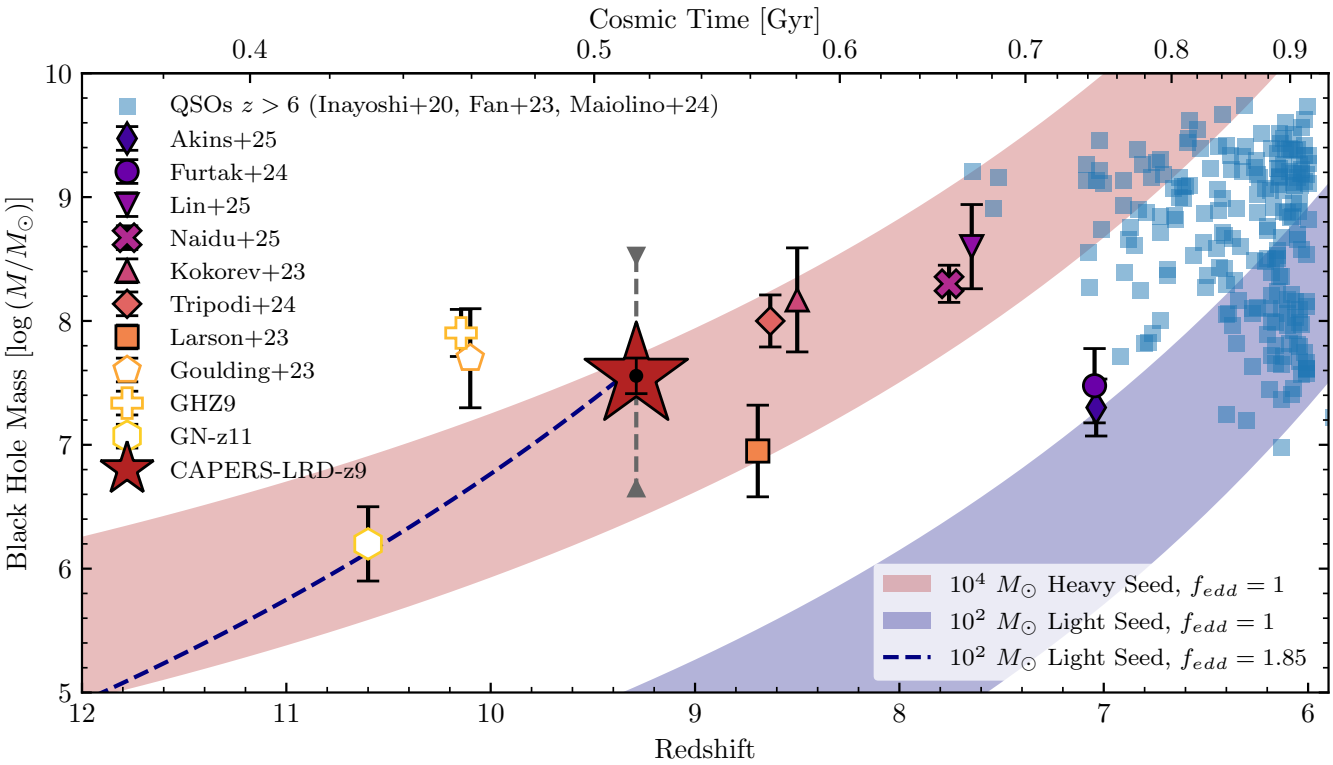

Figure 6. Redshifts and black hole masses of CAPERS-LRD-z9 (red star; canonical errors are shown in black, systematic upper and lower limits are shown in gray), populations of $z \gtrsim 6$ quasars (small blue points, K. Inayoshi et al. 2020; X. Fan et al. 2023; R. Maiolino et al. 2024), notable massive $z > 6$ spectroscopically confirmed BLAGN, (solid symbols, H. B. Akins et al. 2025a; L. J. Furtak et al. 2024; X. Lin et al. 2025; R. P. Naidu et al. 2025; V. Kokorev et al. 2023; R. Tripodi et al. 2024; R. L. Larson et al. 2023), and the highest redshift AGN detected through X-ray emission and high-ionization UV emission lines, respectively (unfilled symbols, A. D. Goulding et al. 2023; A. J. Bunker et al. 2023; O. E. Kovács et al. 2024; L. Napolitano et al. 2025). We also show the growth of $10^2 M_\odot$ (blue shading) and $10^4 M_\odot$ (red shading) black hole seeds growing at the Eddington limit. We also show the growth track of a $10^2 M_\odot$ stellar remnant formed at $z = 30$ that starts accreting at $1.85\times$ the Eddington limit 100 Myrs after formation (dark blue dashed curve). CAPERS-LRD-z9's black hole is too massive to be the result of an Eddington-limited stellar seed, thus a stellar remnant light seed undergoing periods of super-Eddington accretion or a heavy seed are necessary to produce CAPERS-LRD-z9's black hole by $z = 9.288$.

et al. 2025). However, we plot the simplified average Eddington ratio growth curve here for visual clarity.

5.2. *A Dense Gas Origin?*

As referenced in §1, the "dense-gas" model of LRDs has garnered significant attention in the literature in recent months. This model, introduced by K. Inayoshi & R. Maiolino (2025), has recently been applied to two newly discovered LRDs—MoM-150135 at $z = 7.76$ (R. P. Naidu et al. 2025) and RUBIES-UDS-154183 at $z = 3.55$ (A. de Graaff et al. 2025)—as well as the triply-imaged $z = 7.04$ LRD Abell2744-QSO1 (L. J. Furtak et al. 2024; X. Ji et al. 2025). We plot these objects, and the $z = 4.47$ LRD (UNCOVER-45924) from I. Labbe et al. (2024), in Figure 7. All spectra are normalized to the spectrum of CAPERS-LRD-z9 at rest-frame 0.51μm.

All of these objects are notable for their strong Balmer breaks, which, in the cases of MoM-150135 and RUBIES-UDS-154183, were insufficiently fit by evolved stellar populations (R. P. Naidu et al. 2025; A. de Graaff et al. 2025). The Balmer breaks and SEDs of both objects were better fit by invoking the dense-gas model of K. Inayoshi & R. Maiolino (2025). Similarly, while another object—A2744-45924—can be fit with a stellar model, the implied stellar mass is large ($\sim 10^{11}\,M_\odot$) and in tension with ALMA dynamical mass measurement $\sim 10^9\,M_\odot$ (H. B. Akins et al. 2025b).

While CAPERS-LRD-z9 shows a factor of $\sim$ 1.5 softer break $\left(f_{\nu,4050\text{Å}}/f_{\nu,3670\text{Å}} = 4.35^{+0.93}_{-0.67}\right)$ than MoM-150135 ($7.7^{+2.3}_{-1.4}$) and RUBIES-UDS-154183 ($6.9^{+2.8}_{-1.5}$), all of these objects show a remarkably similar rest-frame optical SED and Balmer break shape, suggesting common physical and emission structures. However, unlike MoM-

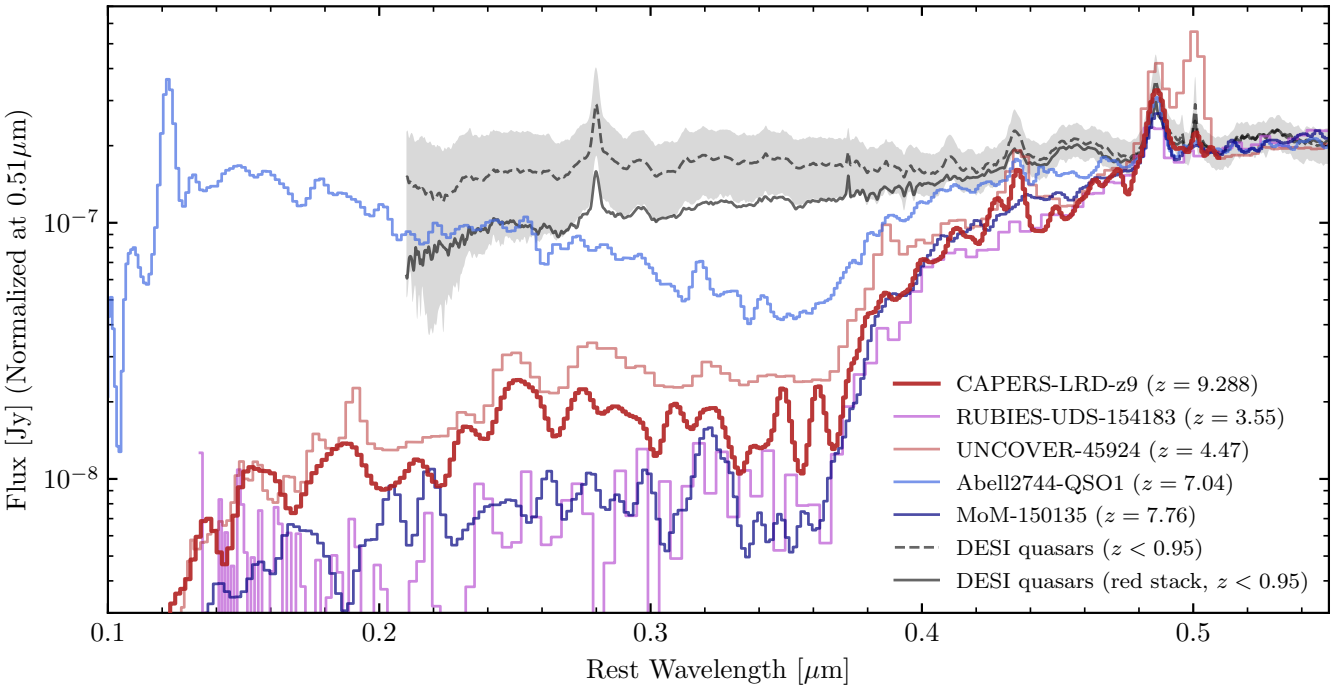

Figure 7. The NIRSpec MSA/PRISM spectra of CAPERS-LRD-z9, MoM-150135 at $z = 7.76$ (R. P. Naidu et al. 2025), RUBIES-UDS-154183 at $z = 3.55$ (A. de Graaff et al. 2025), UNCOVER-45924 at $z = 4.47$ (I. Labbe et al. 2024), and Abell2744-QSO1 at $= 7.04$ (L. J. Furtak et al. 2024; X. Ji et al. 2025) normalized to the spectrum of CAPERS-LRD-z9 at rest-frame 0.51μm. We apply a 1–2 pixel Gaussian smoothing (smoothing lower-z objects less as they are already relatively smoothed by the PRISM's lower spectral resolution at bluer observed wavelengths) to all five spectra to increase visual clarity. For comparison, we plot the median and 10th–90th percentile of DESI spectra of 232 quasars ($z < 0.95$) selected to have similar values of Hβ_{broad} FWHM, L([O III]λ5007), and [O III]λ5007/Hβ flux ratio (gray shading and gray dashed curve), and the stack of the reddest 20 DESI quasars (gray solid curve). While the rest-optical emission from CAPERS-LRD-z9 strongly resembles that of the other NIRSpec sources, these sources are all starkly different from quasars identified in DESI, where even the reddest DESI quasars fail to approach the reddening or Balmer break exhibited in the NIRSpec LRDs.

150135, CAPERS-LRD-z9 demonstrates only moderate Hβ absorption and shows a strong detection of Hγ in emission. Higher resolution spectroscopy of CAPERS-LRD-z9 beyond that of NIRSpec/PRISM would allow for a higher fidelity examination of these features.

Given the similarity in spectral shapes between CAPERS-LRD-z9 and the sources in R. P. Naidu et al. (2025) and A. de Graaff et al. (2025), we propose that the rest-frame optical light from CAPERS-LRD-z9 is indeed dominated by AGN emission through a shell of dense ($\gtrsim 10^{10}$ cm^{-3}) neutral gas, and that the rest-UV emission blue-ward of the Balmer break may be stellar emission from the host galaxy (e.g. D. D. Kocevski et al. 2023) or scattered light, originating from the AGN (e.g. J. E. Greene et al. 2024). From our `CLOUDY` modeling, we infer a gas density of $\log n_H/\mathrm{cm}^{-3} = 9.9^{+0.2}_{-0.2}$ and column density $\log N_H/\mathrm{cm}^{-2} \gtrsim 26$. These results are remarkably comparable to MoM-150135 and RUBIES-UDS-154183, further suggesting that these objects may have similarities in their physical structure.

In terms of the overall assembly history of the first supermassive black holes, we may witness a three-stage evolutionary sequence: the initial seeding process, a period of rapid growth during the LRD stage driven by massive inflows of gas, and a final 'clearing of the fog' (possibly driven by radiation-hydrodynamics processes; e.g., A. Smith et al. 2017), when the emerging SMBHs become unobscured, and with sufficient cosmic time to assemble additional stellar mass, join the 'standard' quasar/AGN sequences at lower redshifts. More specifically, K. Inayoshi (2025) propose that LRDs may be simply the first incidence of AGN activity in a galaxy's evolution, based on the log-normal occurrence rate of LRDs with cosmic time. The nascent evolutionary stage of the LRDs in this toy model may also explain their unique and extreme characteristics. The SMBH could form early in a galaxy's lifespan, surrounded by a large reservoir of dense neutral gas, which serves as both a readily available supply of accretion material and as the shell of dense gas surrounding the AGN (as in K. Inayoshi & R. Maiolino 2025). This scenario would result

in an over-massive SMBH producing a dense-gas reddened SED with a strong Balmer break, in combination with nascent star formation in the host galaxy that produces a blue rest-UV slope. In summation, these two components would supply the two halves of the defining LRD "v-shaped" SED for the duration of the initial "LRD-phase" of AGN activity. Given the low metallicity/dust content, but high column density of the nuclear gas, this model also favorably reproduces the lack of mid-infrared dust emission (C. C. Williams et al. 2024; P. G. Pérez-González et al. 2024; H. B. Akins et al. 2024; G. C. K. Leung et al. 2024), and lack of X-rays (M. Yue et al. 2024a; R. Maiolino et al. 2025; E. Lambrides et al. 2024) observed in LRDs. During future AGN active periods—after a period of dormancy—the stellar mass of the galaxy will have had sufficient time to accumulate and produce a more typical black hole to stellar mass ratio of $M_{\rm BH}/M_* = 0.1\%$. Simultaneously, the dense gas near the AGN would either be blown out by feedback from the AGN during the LRD-phase (as evidenced in velocity offset absorption features exhibited in the Balmer lines of LRDs e.g., J. Matthee et al. 2024; D. D. Kocevski et al. 2025; A. J. Taylor et al. 2024; B. Wang et al. 2024a) or consumed by the AGN during the LRD-phase, such that in future instances of AGN activity, the resulting evolved galaxy and AGN resemble a classical quasar/AGN.

5.3. *A non-stellar origin for the UV continuum?*

In §4.3 we have estimated the stellar mass of the host galaxy of CAPERS-LRD-z9 under the assumption that its UV luminosity is primarily powered by star formation. Even a visual inspection, however, shows that the shape of the UV continuum is unlike that of star-forming galaxies at comparable redshifts, (e.g., M. Castellano et al. 2022; V. Kokorev et al. 2025). As Figure 7 illustrates, despite the relatively low SNR, the slope of the continuum of CAPERS-LRD-z9 appears to change at around rest-frame ≈ 2500 Å, redward of which is relatively blue and rising toward shorter wavelength, whereas at bluer wavelengths it flattens and then perhaps decreases. Moreover, at rest-frame ≈ 2500 Å (observed-frame 2.6 μm) there is a hint of an apparent broad emission feature (see Figs. 1,4). Figure 7 also shows an overall similarity between the UV continuum of CAPERS-LRD-z9 and that of UNCOVER-45924, which has a substantially higher SNR, and strong UV lines such as C IV λ1550 and C III] λ1908 and Fe II lines commonly seen in quasars (e.g. M. Vestergaard & B. J. Wilkes 2001). These features are not detected with statistical significance in the spectrum of CAPERS-LRD-z9, yet the broad emission feature at ≈ 2500 Å may be associated with the Fe II pseudocontinuum, as in A2744-45924. This, as well as the overall shape of the continuum, are intriguing and add credence to the idea that the UV continuum in CAPERS-LRD-z9 could be non-stellar.

To further explore this idea, we compare the LRDs to a control sample of quasars ($z < 0.95$) from the Dark Energy Spectroscopic Instrument (DESI) DR1 dataset (DESI Collaboration et al. 2025). We assemble this sample by selecting DESI quasars with similar H$\beta_{\rm broad}$ FWHM, L([O III]λ5007), and [O III]λ5007/H$\beta_{\rm total}$ flux ratios to CAPERS-LRD-z9 based on `FastSpecFit` (J. Moustakas et al. 2023) emission-line measurements reported in the DESI AGN/QSO value-added catalog[36] (S. Juneau et al., in preparation). We plot both the 10th–90th percentile of these objects as well as the inverse-variance weighted mean stack of the 20 reddest objects in Figure 7 as a standard of comparison. It is immediately clear that even the stack of the reddest DESI quasars strongly differs from the LRD rest-optical continua, including a lack of the prominent Fe II bump at 4434–4684Å in the LRDs (which is not expected to appear in faint [$L_{\rm H\beta} < 10^{44}$ erg s^{-1}] high-redshift AGN e.g., B. Trefoloni et al. 2024). However, as mentioned above, in the rest-UV, CAPERS-LRD-z9 and UNCOVER-45924 both exhibit possible AGN-signature emission features such as the $\sim 0.25\mu$m iron bump, prominently featured in the DESI stack, suggesting that the rest-UV emission may indeed have an AGN origin.

The question naturally arises how UV emission from the accretion disk can escape such a dense gas cloud. As suggested by J. E. Greene et al. (2024), the rest-UV light in LRDs could originate from accretion disk photons either being scattered or directly transmitted (via a patchy medium). If we simply re-scale the rest-UV continuum from the DESI quasars shown in Figure 7 to match our data, we find that the UV slopes are roughly consistent with an implied scattering fraction of $\sim$10%, fully consistent with the results presented in J. E. Greene et al. (2024). The scattering medium could be neutral (Rayleigh scattering) or partially ionized gas (Rayleigh and Thomson scattering), and could be associated with either the external regions of the same dense gaseous envelope that enshrouds the AGN or a different regions altogether. The type of scattering medium and its geometry will, in general, contribute to the overall spectral shape and intensity, given the specific wavelength-dependence of the scattered radiation,

[36] https://data.desi.lbl.gov/doc/releases/dr1/vac/agnqso/

and this might also help explain the diversity of spectral morphologies observed this category of sources.

If the UV emission is predominantly of AGN origin, the upper limit to the stellar mass discussed in §4.3 will have to be revised downward by a substantial amount, which is unconstrained by the current data. This makes the ratio $M_{BH}/M_* \gg 4.5\%$ substantially more extreme, with important implications on the mechanisms of formation and co-evolution of SMBHs and their host galaxies.

6. SUMMARY

In this work we spectroscopically confirm and analyze the highest redshift BLAGN observed to date: CAPERS-LRD-z9. We summarize our primary results below:

1. Using *JWST*/NIRSpec PRISM spectroscopy from the CAPERS program, we identify the highest redshift ($z = 9.288$) BLAGN yet discovered—CAPERS-LRD-z9—based on a strong detection of broad (FWHM=3525 ± 589 km s^{-1}) Hβ emission.

2. We determine that CAPERS-LRD-z9 is unresolved in NIRCam imaging, placing upper limits of $\lesssim 175$ pc and $\lesssim 350$ pc on its physical size in the rest-UV and rest-optical.

3. We use the J. E. Greene & L. C. Ho (2005) empirical relations to estimate a black hole mass of $\log(M_{\rm BH}/M_\odot) = 7.58 \pm 0.15$. We place conservative bounds on this mass measurement, accounting for systematic uncertainties, by assuming Eddington-limited accretion (lower bound) and applying a dust correction based on the Balmer decrement (upper bound). This yields a range of $\log(M_{\rm BH}/M_\odot) = 6.65$–$8.50$.

4. We successfully model CAPERS-LRD-z9 as an AGN enshrouded in a shell of dense ($n_H > 10^9$ cm^{-3}) neutral gas using `CLOUDY` following the models of K. Inayoshi & R. Maiolino (2025) that have been recently applied to similar sources (X. Ji et al. 2025; R. P. Naidu et al. 2025; A. de Graaff et al. 2025). We fit the rest-frame UV to a stellar population model using `bagpipes`. From this modeling, we derive an upper limit on the host galaxy stellar mass of $< 10^9 M_\odot$ and estimate a neutral gas density near the AGN of $n_H \sim 10^{10}$ cm^{-3}.

5. From our canonical black hole mass, we calculate a black hole mass to stellar mass ratio $M_{\rm BH}/M_* > 4.5\%$ for CAPERS-LRD-z9. However, we recognize our estimates of both $M_{\rm BH}$ and M_* are subject to large systematic uncertainties. Based on our systematic bounds of $M_{\rm BH}$, the lower limit on $M_{\rm BH}/M_*$ ranges from $>46\%$ to as low as $>0.5\%$. Even our absolute lowest bound presents a significant deviation from the "typical" $M_{\rm BH}/M_* \sim 0.1\%$ value exhibited by local quasars.

6. We model the growth of the SMBH powering CAPERS-LRD-z9 and find that an Eddington-limited heavy ($\sim 10^4 M_\odot$) seed or a super-Eddington light ($\sim 10^2 M_\odot$) seed are necessary to produce such a SMBH by $z = 9.288$.

From these results, it is clear that CAPERS-LRD-z9 is an extreme example of an LRD in redshift, $M_{\rm BH}/M_*$, and neutral gas density. Along with MoM-150135 and RUBIES-UDS-154183, CAPERS-LRD-z9 provides strong evidence in support of the "dense-gas enshrouded AGN" physical explanation for the rest-frame optical emission from LRDs. Furthermore, its unprecedented redshift for a BLAGN provides insight into the interplay between black hole formation and growth and the physical properties of LRDs. While we present an initial analysis of CAPERS-LRD-z9 in this work, further analysis of such an exotic source will undoubtedly continue to enhance our understanding of galaxy, AGN, and SMBH evolution in the very early universe.

ACKNOWLEDGEMENTS

AJT acknowledges support from the UT Austin College of Natural Sciences, and AJT and SLF acknowledge support from STScI/NASA through JWST-GO-6368. ACC acknowledges support from a UKRI Frontier Research Guarantee Grant (PI Carnall; grant reference EP/Y037065/1). LN acknowledges support from grant "Progetti per Avvio alla Ricerca - Tipo 1, Unveiling Cosmic Dawn: Galaxy Evolution with CAPERS" (AR1241906F947685). JSD acknowledges the support of the Royal Society via the award of a Royal Society Research Professorship. RA acknowledges support of Grant PID2023-147386NB-I00 funded by MICIU/AEI/10.13039/501100011033 and by ERDF/EU, and the Severo Ochoa grant CEX2021-001131-S funded by MCIN/AEI/10.13039/50110001103. FC and TMS acknowledge support from a UKRI Frontier Research Guarantee Grant (PI Cullen; grant reference EP/X021025/1).

This research used data obtained with the Dark Energy Spectroscopic Instrument (DESI). DESI construction and operations is managed by the Lawrence Berke-

ley National Laboratory. This material is based upon work supported by the U.S. Department of Energy, Office of Science, Office of High-Energy Physics, under Contract No. DE–AC02–05CH11231, and by the National Energy Research Scientific Computing Center, a DOE Office of Science User Facility under the same contract. Additional support for DESI was provided by the U.S. National Science Foundation (NSF), Division of Astronomical Sciences under Contract No. AST-0950945 to the NSF National Optical-Infrared Astronomy Research Laboratory; the Science and Technology Facilities Council of the United Kingdom; the Gordon and Betty Moore Foundation; the Heising-Simons Foundation; the French Alternative Energies and Atomic Energy Commission (CEA); the National Council of Humanities, Science and Technology of Mexico (CONAHCYT); the Ministry of Science and Innovation of Spain (MICINN), and by the DESI Member Institutions: www.desi.lbl.gov/collaborating-institutions. The DESI collaboration is honored to be permitted to conduct scientific research on I'oligam Du'ag (Kitt Peak), a mountain with particular significance to the Tohono O'odham Nation.

We also acknowledge Haojie Hu for kindly sharing the data from their black hole seeding and growth model, which we use in Figure 5 for comparison with our observational results.

The uncalibrated data are available at MAST: doi: 10.17909/0q3p-sp24

Facilities: JWST

Software: astropy: Astropy Collaboration et al. (2013, 2018, 2022), bagpipes: A. C. Carnall et al. (2018), CLOUDY: M. Chatzikos et al. (2023), emcee: D. Foreman-Mackey et al. (2013), JWST pipeline: H. Bushouse et al. (2025), scipy: P. Virtanen et al. (2020), SPARCL: S. Juneau et al. (2024)

REFERENCES

Abuter, R., Allouche, F., Amorim, A., et al. 2024, Nature, 627, 281, doi: 10.1038/s41586-024-07053-4

Adamo, A., Bradley, L. D., Vanzella, E., et al. 2024, Nature, 632, 513, doi: 10.1038/s41586-024-07703-7

Agarwal, B., Davis, A. J., Khochfar, S., Natarajan, P., & Dunlop, J. S. 2013, MNRAS, 432, 3438, doi: 10.1093/mnras/stt696

Akins, H. B., Casey, C. M., Lambrides, E., et al. 2024, arXiv e-prints, arXiv:2406.10341, doi: 10.48550/arXiv.2406.10341

Akins, H. B., Casey, C. M., Berg, D. A., et al. 2025a, ApJL, 980, L29, doi: 10.3847/2041-8213/adab76

Akins, H. B., Casey, C. M., Chisholm, J., et al. 2025b, arXiv e-prints, arXiv:2503.00998, doi: 10.48550/arXiv.2503.00998

Arrabal Haro, P., Dickinson, M., Finkelstein, S. L., et al. 2023, ApJL, 951, L22, doi: 10.3847/2041-8213/acdd54

Astropy Collaboration, Robitaille, T. P., Tollerud, E. J., et al. 2013, A&A, 558, A33, doi: 10.1051/0004-6361/201322068

Astropy Collaboration, Price-Whelan, A. M., SipHocz, B. M., et al. 2018, AJ, 156, 123, doi: 10.3847/1538-3881/aabc4f

Astropy Collaboration, Price-Whelan, A. M., Lim, P. L., et al. 2022, ApJ, 935, 167, doi: 10.3847/1538-4357/ac7c74

Backhaus, B. E., Bridge, J. S., Trump, J. R., et al. 2023, ApJ, 943, 37, doi: 10.3847/1538-4357/aca668

Baggen, J. F. W., van Dokkum, P., Brammer, G., et al. 2024, arXiv e-prints, arXiv:2408.07745, doi: 10.48550/arXiv.2408.07745

Barro, G., Perez-Gonzalez, P. G., Kocevski, D. D., et al. 2023, arXiv e-prints, arXiv:2305.14418, doi: 10.48550/arXiv.2305.14418

Barro, G., Perez-Gonzalez, P. G., Kocevski, D. D., et al. 2024, arXiv e-prints, arXiv:2412.01887, doi: 10.48550/arXiv.2412.01887

Barvainis, R. 1987, ApJ, 320, 537, doi: 10.1086/165571

Begelman, M. C., Volonteri, M., & Rees, M. J. 2006, MNRAS, 370, 289, doi: 10.1111/j.1365-2966.2006.10467.x

Bentz, M. C., Onken, C. A., Street, R., & Valluri, M. 2023, ApJ, 944, 29, doi: 10.3847/1538-4357/acab62

Bentz, M. C., Peterson, B. M., Pogge, R. W., Vestergaard, M., & Onken, C. A. 2006, ApJ, 644, 133, doi: 10.1086/503537

Bhowmick, A. K., Blecha, L., Torrey, P., et al. 2024, MNRAS, 533, 1907, doi: 10.1093/mnras/stae1819

Brammer, G. 2022,, 0.3 doi: 10.5281/zenodo.7299500

Brammer, G. B., van Dokkum, P. G., & Coppi, P. 2008, ApJ, 686, 1503, doi: 10.1086/591786

Brinchmann, J. 2023, MNRAS, 525, 2087, doi: 10.1093/mnras/stad1704

Bromm, V., & Loeb, A. 2003, ApJ, 596, 34, doi: 10.1086/377529

Brooks, M., Simons, R. C., Trump, J. R., et al. 2024, arXiv e-prints, arXiv:2410.07340, doi: 10.48550/arXiv.2410.07340

Bunker, A. J., Saxena, A., Cameron, A. J., et al. 2023, A&A, 677, A88, doi: 10.1051/0004-6361/202346159

Bushouse, H., Eisenhamer, J., Dencheva, N., et al. 2025,, 1.18.0 Zenodo, doi: 10.5281/zenodo.6984365

Cackett, E. M., Bentz, M. C., & Kara, E. 2021, iScience, 24, 102557, doi: 10.1016/j.isci.2021.102557

Capak, P. L., Carilli, C., Jones, G., et al. 2015, Nature, 522, 455, doi: 10.1038/nature14500

Carnall, A. C., McLure, R. J., Dunlop, J. S., & Davé, R. 2018, MNRAS, 480, 4379, doi: 10.1093/mnras/sty2169

Carniani, S., Hainline, K., D'Eugenio, F., et al. 2024, Nature, 633, 318, doi: 10.1038/s41586-024-07860-9

Castellano, M., Fontana, A., Treu, T., et al. 2022, ApJL, 938, L15, doi: 10.3847/2041-8213/ac94d0

Chatzikos, M., Bianchi, S., Camilloni, F., et al. 2023, RMxAA, 59, 327, doi: 10.22201/ia.01851101p.2023.59.02.12

Chen, C.-H., Ho, L. C., Li, R., & Zhuang, M.-Y. 2025, ApJ, 983, 60, doi: 10.3847/1538-4357/ada93a

Chon, S., & Omukai, K. 2025, MNRAS, 539, 2561, doi: 10.1093/mnras/staf598

Cullen, F., Carnall, A. C., Scholte, D., et al. 2025, arXiv e-prints, arXiv:2501.11099, doi: 10.48550/arXiv.2501.11099

de Graaff, A., Rix, H.-W., Naidu, R. P., et al. 2025, arXiv e-prints, arXiv:2503.16600, doi: 10.48550/arXiv.2503.16600

de Graaff, A. G., Brammer, G., Bezanson, R., et al. 2023,, JWST Proposal. Cycle 2, ID. #4233

DESI Collaboration, Abdul-Karim, M., Adame, A. G., et al. 2025, arXiv e-prints, arXiv:2503.14745, doi: 10.48550/arXiv.2503.14745

Donnan, C. T., McLure, R. J., Dunlop, J. S., et al. 2024, MNRAS, 533, 3222, doi: 10.1093/mnras/stae2037

Du, P., Lu, K.-X., Zhang, Z.-X., et al. 2016, ApJ, 825, 126, doi: 10.3847/0004-637X/825/2/126

Dunlop, J. S., Abraham, R. G., Ashby, M. L. N., et al. 2021,, JWST Proposal. Cycle 1, ID. #1837

Fan, X., Bañados, E., & Simcoe, R. A. 2023, ARA&A, 61, 373, doi: 10.1146/annurev-astro-052920-102455

Finkelstein, S. L., & Bagley, M. B. 2022, ApJ, 938, 25, doi: 10.3847/1538-4357/ac89eb

Finkelstein, S. L., Bagley, M. B., Arrabal Haro, P., et al. 2022, ApJL, 940, L55, doi: 10.3847/2041-8213/ac966e

Finkelstein, S. L., Leung, G. C. K., Bagley, M. B., et al. 2024, ApJL, 969, L2, doi: 10.3847/2041-8213/ad4495

Finkelstein, S. L., Bagley, M. B., Arrabal Haro, P., et al. 2025, arXiv e-prints, arXiv:2501.04085, doi: 10.48550/arXiv.2501.04085

Fonseca Alvarez, G., Trump, J. R., Homayouni, Y., et al. 2020, ApJ, 899, 73, doi: 10.3847/1538-4357/aba001

Foreman-Mackey, D., Hogg, D. W., Lang, D., & Goodman, J. 2013, PASP, 125, 306, doi: 10.1086/670067

Fries, L. B., Trump, J. R., Horne, K., et al. 2024, ApJ, 975, 239, doi: 10.3847/1538-4357/ad7c42

Fujimoto, S., Ouchi, M., Kohno, K., et al. 2024, arXiv e-prints, arXiv:2402.18543, doi: 10.48550/arXiv.2402.18543

Furtak, L. J., Labbé, I., Zitrin, A., et al. 2024, Nature, 628, 57, doi: 10.1038/s41586-024-07184-8

Gordon, K. D., Clayton, G. C., Misselt, K. A., Landolt, A. U., & Wolff, M. J. 2003, ApJ, 594, 279, doi: 10.1086/376774

Goulding, A. D., Greene, J. E., Setton, D. J., et al. 2023, ApJL, 955, L24, doi: 10.3847/2041-8213/acf7c5

Greene, J. E., & Ho, L. C. 2005, ApJ, 630, 122, doi: 10.1086/431897

Greene, J. E., Labbe, I., Goulding, A. D., et al. 2024, ApJ, 964, 39, doi: 10.3847/1538-4357/ad1e5f

Grogin, N. A., Kocevski, D. D., Faber, S. M., et al. 2011, ApJS, 197, 35, doi: 10.1088/0067-0049/197/2/35

Harikane, Y., Zhang, Y., Nakajima, K., et al. 2023, ApJ, 959, 39, doi: 10.3847/1538-4357/ad029e

Hopkins, A. M. 2004, ApJ, 615, 209, doi: 10.1086/424032

Horne, K. 1986, PASP, 98, 609, doi: 10.1086/131801

Hu, H., Inayoshi, K., Haiman, Z., Ho, L. C., & Ohsuga, K. 2025, ApJL, 983, L37, doi: 10.3847/2041-8213/adc680

Inayoshi, K. 2025, arXiv e-prints, arXiv:2503.05537, doi: 10.48550/arXiv.2503.05537

Inayoshi, K., & Maiolino, R. 2025, ApJL, 980, L27, doi: 10.3847/2041-8213/adaebd

Inayoshi, K., Visbal, E., & Haiman, Z. 2020, ARA&A, 58, 27, doi: 10.1146/annurev-astro-120419-014455

Isobe, Y., Ouchi, M., Nakajima, K., et al. 2023, arXiv e-prints, arXiv:2301.06811, doi: 10.48550/arXiv.2301.06811

Jeon, J., Bromm, V., Liu, B., & Finkelstein, S. L. 2025a, ApJ, 979, 127, doi: 10.3847/1538-4357/ad9f3a

Jeon, J., Liu, B., Taylor, A. J., et al. 2025b, arXiv e-prints, arXiv:2503.14703, doi: 10.48550/arXiv.2503.14703

Ji, X., Maiolino, R., Übler, H., et al. 2025, arXiv e-prints, arXiv:2501.13082, doi: 10.48550/arXiv.2501.13082

Johnson, J. L., & Bromm, V. 2007, MNRAS, 374, 1557, doi: 10.1111/j.1365-2966.2006.11275.x

Juneau, S., Jacques, A., Pothier, S., et al. 2024, arXiv e-prints, arXiv:2401.05576, doi: 10.48550/arXiv.2401.05576

Juodžbalis, I., Ji, X., Maiolino, R., et al. 2024, MNRAS, 535, 853, doi: 10.1093/mnras/stae2367

Juodžbalis, I., Maiolino, R., Baker, W. M., et al. 2025, arXiv e-prints, arXiv:2504.03551, doi: 10.48550/arXiv.2504.03551

Katz, H., Saxena, A., Cameron, A. J., et al. 2023, MNRAS, 518, 592, doi: 10.1093/mnras/stac2657

Kocevski, D. D., Onoue, M., Inayoshi, K., et al. 2023, ApJL, 954, L4, doi: 10.3847/2041-8213/ace5a0

Kocevski, D. D., Finkelstein, S. L., Barro, G., et al. 2025, arXiv e-prints, arXiv:2404.03576, doi: 10.48550/arXiv.2404.03576

Koekemoer, A. M., Faber, S. M., Ferguson, H. C., et al. 2011, ApJS, 197, 36, doi: 10.1088/0067-0049/197/2/36

Kokorev, V., Fujimoto, S., Labbe, I., et al. 2023, ApJL, 957, L7, doi: 10.3847/2041-8213/ad037a

Kokorev, V., Caputi, K. I., Greene, J. E., et al. 2024a, ApJ, 968, 38, doi: 10.3847/1538-4357/ad4265

Kokorev, V., Chisholm, J., Endsley, R., et al. 2024b, arXiv e-prints, arXiv:2407.20320, doi: 10.48550/arXiv.2407.20320

Kokorev, V., Chávez Ortiz, Ó. A., Taylor, A. J., et al. 2025, arXiv e-prints, arXiv:2504.12504, doi: 10.48550/arXiv.2504.12504

Korista, K. T., & Goad, M. R. 2004, ApJ, 606, 749, doi: 10.1086/383193

Kovács, O. E., Bogdán, Á., Natarajan, P., et al. 2024, ApJL, 965, L21, doi: 10.3847/2041-8213/ad391f

Labbé, I., van Dokkum, P., Nelson, E., et al. 2023, Nature, 616, 266, doi: 10.1038/s41586-023-05786-2

Labbe, I., Greene, J. E., Matthee, J., et al. 2024, arXiv e-prints, arXiv:2412.04557, doi: 10.48550/arXiv.2412.04557

Lambrides, E., Garofali, K., Larson, R., et al. 2024, arXiv e-prints, arXiv:2409.13047, doi: 10.48550/arXiv.2409.13047

Larson, R. L., Finkelstein, S. L., Kocevski, D. D., et al. 2023, ApJL, 953, L29, doi: 10.3847/2041-8213/ace619

Lauer, T. R., Tremaine, S., Richstone, D., & Faber, S. M. 2007, ApJ, 670, 249, doi: 10.1086/522083

Leung, G. C. K., Finkelstein, S. L., Pérez-González, P. G., et al. 2024, arXiv e-prints, arXiv:2411.12005, doi: 10.48550/arXiv.2411.12005

Li, J., Silverman, J. D., Shen, Y., et al. 2025, ApJ, 981, 19, doi: 10.3847/1538-4357/ada603

Lin, X., Fan, X., Wang, F., et al. 2025, arXiv e-prints, arXiv:2504.08039, doi: 10.48550/arXiv.2504.08039

Liu, B., & Bromm, V. 2022, ApJL, 937, L30, doi: 10.3847/2041-8213/ac927f

Lupi, A., Trinca, A., Volonteri, M., Dotti, M., & Mazzucchelli, C. 2024, A&A, 689, A128, doi: 10.1051/0004-6361/202451249

Luridiana, V., Morisset, C., & Shaw, R. A. 2015, A&A, 573, A42, doi: 10.1051/0004-6361/201323152

Lyu, J., & Rieke, G. 2022, Universe, 8, 304, doi: 10.3390/universe8060304

Maiolino, R., Scholtz, J., Curtis-Lake, E., et al. 2023, arXiv e-prints, arXiv:2308.01230, doi: 10.48550/arXiv.2308.01230

Maiolino, R., Scholtz, J., Curtis-Lake, E., et al. 2024, A&A, 691, A145, doi: 10.1051/0004-6361/202347640

Maiolino, R., Risaliti, G., Signorini, M., et al. 2025, MNRAS, 538, 1921, doi: 10.1093/mnras/staf359

Matteri, A., Ferrara, A., & Pallottini, A. 2025, arXiv e-prints, arXiv:2503.18850, doi: 10.48550/arXiv.2503.18850

Matthee, J., Naidu, R. P., Brammer, G., et al. 2024, ApJ, 963, 129, doi: 10.3847/1538-4357/ad2345

Mazzolari, G., Übler, H., Maiolino, R., et al. 2024, A&A, 691, A345, doi: 10.1051/0004-6361/202450407

Moustakas, J., Scholte, D., Dey, B., & Khederlarian, A. 2023,, Astrophysics Source Code Library, record ascl:2308.005 http://ascl.net/2308.005

Mowla, L., Iyer, K., Asada, Y., et al. 2024, arXiv e-prints, arXiv:2402.08696, doi: 10.48550/arXiv.2402.08696

Naidu, R. P., Oesch, P. A., van Dokkum, P., et al. 2022, ApJL, 940, L14, doi: 10.3847/2041-8213/ac9b2210.48550/arXiv.2207.09434

Naidu, R. P., Matthee, J., Katz, H., et al. 2025, arXiv e-prints, arXiv:2503.16596, doi: 10.48550/arXiv.2503.16596

Napolitano, L., Castellano, M., Pentericci, L., et al. 2025, A&A, 693, A50, doi: 10.1051/0004-6361/202452090

Narayanan, D., Lower, S., Torrey, P., et al. 2024, ApJ, 961, 73, doi: 10.3847/1538-4357/ad0966

Omukai, K., Schneider, R., & Haiman, Z. 2008, ApJ, 686, 801, doi: 10.1086/591636

Osterbrock, D. E. 1989, Astrophysics of Gaseous Nebulae and Active Galactic Nuclei (University Science Books)

Östlin, G., Pérez-González, P. G., Melinder, J., et al. 2025, A&A, 696, A57, doi: 10.1051/0004-6361/202451723

Pacucci, F., Nguyen, B., Carniani, S., Maiolino, R., & Fan, X. 2023, ApJL, 957, L3, doi: 10.3847/2041-8213/ad0158

Peng, C. Y., Ho, L. C., Impey, C. D., & Rix, H.-W. 2002, AJ, 124, 266, doi: 10.1086/340952

Pérez-González, P. G., Rieke, G. H., Villar, V., et al. 2008, ApJ, 675, 234, doi: 10.1086/523690

Pérez-González, P. G., Costantin, L., Langeroodi, D., et al. 2023, ApJL, 951, L1, doi: 10.3847/2041-8213/acd9d0

Pérez-González, P. G., Barro, G., Rieke, G. H., et al. 2024, ApJ, 968, 4, doi: 10.3847/1538-4357/ad38bb

Reddy, N. A., Kriek, M., Shapley, A. E., et al. 2015, ApJ, 806, 259, doi: 10.1088/0004-637X/806/2/259

Reddy, N. A., Oesch, P. A., Bouwens, R. J., et al. 2018, ApJ, 853, 56, doi: 10.3847/1538-4357/aaa3e7

Regan, J., & Volonteri, M. 2024, The Open Journal of Astrophysics, 7, 72, doi: 10.33232/001c.123239

Robertson, B. E., Tacchella, S., Johnson, B. D., et al. 2023, Nature Astronomy, 7, 611, doi: 10.1038/s41550-023-01921-1

Rusakov, V., Watson, D., Nikopoulos, G. P., et al. 2025, arXiv e-prints, arXiv:2503.16595, doi: 10.48550/arXiv.2503.16595

Setton, D. J., Greene, J. E., de Graaff, A., et al. 2024, arXiv e-prints, arXiv:2411.03424, doi: 10.48550/arXiv.2411.03424

Smith, A., Becerra, F., Bromm, V., & Hernquist, L. 2017, MNRAS, 472, 205, doi: 10.1093/mnras/stx1993

Smith, A., & Bromm, V. 2019, Contemporary Physics, 60, 111, doi: 10.1080/00107514.2019.1615715

Stanway, E. R., & Eldridge, J. J. 2018, MNRAS, 479, 75, doi: 10.1093/mnras/sty1353

Stern, J., & Laor, A. 2012, MNRAS, 423, 600, doi: 10.1111/j.1365-2966.2012.20901.x

Storey, P. J., & Zeippen, C. J. 2000, MNRAS, 312, 813, doi: 10.1046/j.1365-8711.2000.03184.x

Suh, H., Scharwächter, J., Farina, E. P., et al. 2025, Nature Astronomy, 9, 271, doi: 10.1038/s41550-024-02402-9

Tacchella, S., Johnson, B. D., Robertson, B. E., et al. 2022, MNRAS, submitted. https://arxiv.org/abs/2208.03281

Takeo, E., Inayoshi, K., & Mineshige, S. 2020, MNRAS, 497, 302, doi: 10.1093/mnras/staa1906

Taylor, A. J., Finkelstein, S. L., Kocevski, D. D., et al. 2024, arXiv e-prints, arXiv:2409.06772, doi: 10.48550/arXiv.2409.06772

Trefoloni, B., Ji, X., Maiolino, R., et al. 2024, arXiv e-prints, arXiv:2410.21867, doi: 10.48550/arXiv.2410.21867

Trinca, A., Schneider, R., Valiante, R., et al. 2022, MNRAS, 511, 616, doi: 10.1093/mnras/stac062

Tripodi, R., Martis, N., Markov, V., et al. 2024, arXiv e-prints, arXiv:2412.04983, doi: 10.48550/arXiv.2412.04983

U, V., Barth, A. J., Vogler, H. A., et al. 2022, ApJ, 925, 52, doi: 10.3847/1538-4357/ac3d26

Übler, H., Maiolino, R., Pérez-González, P. G., et al. 2024, MNRAS, 531, 355, doi: 10.1093/mnras/stae943

van Hoof, P. A. M. 2018, Galaxies, 6, 63, doi: 10.3390/galaxies6020063

Vestergaard, M., & Wilkes, B. J. 2001, ApJS, 134, 1, doi: 10.1086/320357

Virtanen, P., Gommers, R., Oliphant, T. E., et al. 2020, Nature Methods, 17, 261, doi: 10.1038/s41592-019-0686-2

Volonteri, M., Habouzit, M., & Colpi, M. 2021, Nature Reviews Physics, 3, 732, doi: 10.1038/s42254-021-00364-9

Wang, B., Fujimoto, S., Labbé, I., et al. 2023, ApJL, 957, L34, doi: 10.3847/2041-8213/acfe07

Wang, B., de Graaff, A., Davies, R. L., et al. 2024a, arXiv e-prints, arXiv:2403.02304, doi: 10.48550/arXiv.2403.02304

Wang, B., Leja, J., de Graaff, A., et al. 2024b, ApJL, 969, L13, doi: 10.3847/2041-8213/ad55f7

Williams, C. C., Alberts, S., Ji, Z., et al. 2024, ApJ, 968, 34, doi: 10.3847/1538-4357/ad3f17

Wise, J. H., Regan, J. A., O'Shea, B. W., et al. 2019, Nature, 566, 85, doi: 10.1038/s41586-019-0873-4

Woods, T. E., Agarwal, B., Bromm, V., et al. 2019, PASA, 36, e027, doi: 10.1017/pasa.2019.14

Yue, M., Eilers, A.-C., Ananna, T. T., et al. 2024a, ApJL, 974, L26, doi: 10.3847/2041-8213/ad7eba

Yue, M., Eilers, A.-C., Simcoe, R. A., et al. 2024b, ApJ, 966, 176, doi: 10.3847/1538-4357/ad3914

Zavala, J. A., Castellano, M., Akins, H. B., et al. 2025, Nature Astronomy, 9, 155, doi: 10.1038/s41550-024-02397-3

Zhang, S., Liu, B., Bromm, V., et al. 2025, arXiv e-prints, arXiv:2503.17585, doi: 10.48550/arXiv.2503.17585

Ziparo, F., Gallerani, S., & Ferrara, A. 2025, JCAP, 2025, 040, doi: 10.1088/1475-7516/2025/04/040